Materials Science & Engineering A 974 (2026) 150841

Contents lists available at ScienceDirect

Materials Science & Engineering A

journal homepage: www.elsevier.com/locate/msea

Engineering nanoscale heterogeneities in thin film metallic glasses via alloying with immiscible elements

Evgeniy Boltynjuk [a,*,1], Marco Ezequiel [b,1], Francesco Bignoli [b], Vahid Tavakkoli [a,c], Ali Ahmadian [a], Delphine Chassaing [d,e], Michael Eusterholz [d,e], Fatih Zighem [b], Damien Faurie [b], Philippe Djemia [b], Horst Hahn [a,f], Yulia Ivanisenko [a], Matteo Ghidelli [b]

[a] Institute of Nanotechnology, Karlsruhe Institute of Technology, Eggenstein-Leopoldshafen, 76344, Germany
[b] Laboratoire des Sciences des Procédés et des Matériaux (LSPM), CNRS, Université Sorbonne Paris Nord, Villetaneuse, 93430, France
[c] Department of Materials and Earth Sciences, Technical University of Darmstadt (TUD), Darmstadt, 64287, Germany
[d] Karlsruhe Nano Micro Facility (KNMFi), Karlsruhe Institute of Technology, Eggenstein-Leopoldshafen, 76344, Germany
[e] Institute of Applied Materials (IAM-WK), Karlsruhe Institute of Technology, Hermann-von-Helmholtz-Platz 1, Eggenstein-Leopoldshafen, 76344, Germany
[f] Department of Materials Science and Engineering, University of Arizona, Tucson, United States

ARTICLE INFO

Keywords:
Thin film metallic glasses
Ab initio molecular dynamics
Microstructure
Nanoscale heterogeneity
Mechanical properties

ABSTRACT

Controlling nanoscale heterogeneity in metallic glasses offers a promising route to tailor their mechanical behavior. In this work, we investigate $(Zr_{34}Cu_{66})_{100-x}Fe_x$ thin film metallic glasses (TFMGs) across a wide compositional range (x = 0 – 76 at.%) to reveal how immiscibility between Cu and Fe can lead to heterogeneity, thereby influencing their structure and mechanical properties. Guided by thermodynamic modeling, we show that $(Zr_{34}Cu_{66})_{100-x}Fe_x$ retains an amorphous structure up to 77.5 at.% Fe, enabling systematic investigation of a wide range of compositions within ZrCu-rich and Fe-rich regions. *Ab initio* molecular dynamics simulations reveal that Fe addition in the range of 17-29 at.% maximizes the population of highly stable icosahedral <0,0,12,0> motifs, thereby increasing hardness (*H*) from ~7.9 up to ~8.5 GPa, while further Fe increase leads to a reduction in *H* as a result of the weakening of atomic bonds. At 76 at.% Fe, atom probe tomography reveals the presence of Cu-rich amorphous clusters, accompanied by *H* decrement down to ~7.6 GPa. Moreover, we show that nanoscale phase separation in the form of Cu-rich clusters controls the deformation mode, affecting the amplitude of strain rate serrations during nanoindentation, decreasing from ~16 down to ~5 for high Fe content, indicating a transition from localized to more homogeneous plastic flow. Overall, we demonstrate a simple approach to tailor local heterogeneities of TFMGs by introducing immiscible elemental constituents, successfully managing to control the mechanical behavior, which can be beneficial for advanced material applications.

1. Introduction

Metallic glasses (MGs) have attracted attention for their unique combination of high strength and elastic deformation, making them promising candidates for many structural and functional applications [1,2]. However, the absence of long-range structural order leads to plastic deformation localization into narrow (~10 nm) shear bands (SBs) [3,4], initiating a catastrophic brittle failure. One effective strategy to mitigate this behavior is the controlled introduction of local structural heterogeneities [5,6]. Such heterogeneities may originate from variations in short- and medium-range order (SRO and MRO), reflected in distinct Voronoi polyhedra and packing motifs, or from nanoscale or even microscale chemical segregation [5,6]. These heterogeneities act as internal barriers that can deflect or arrest SBs, thereby enhancing the overall plasticity of MGs [7–11]. Moreover, by adjusting their volume fraction, spatial distribution, and chemical composition, it is possible to tailor their mechanical properties, including hardness as well as the strength-ductility balance.

Thin film metallic glasses (TFMGs) are well suited to this purpose, since they can serve both as model systems for fundamental study [12]

* Corresponding author. Institute of Nanotechnology, Karlsruhe Institute of Technology, Hermann-von-Helmholtz-Platz 1, 76344, Eggenstein-Leopoldshafen, Germany.
E-mail address: evgeniy.boltynjuk@kit.edu (E. Boltynjuk).
[1] These authors contributed equally to the work.

https://doi.org/10.1016/j.msea.2026.150841
Received 28 April 2026; Received in revised form 15 July 2026; Accepted 25 July 2026
Available online 26 July 2026

and as practical coating materials [13]. Specifically, the precise control over the synthesis parameters along with the extremely high cooling rate up to 10^{12} K/s during the deposition [14] allows a fine tuning of chemistry and the formation of a glass phase over a wide compositional range [15,16], while simultaneously dictating the degree of nanoscale heterogeneity, manifested in local variations of chemical composition or short-range order.

The control of local heterogeneities in MGs can be carried out through several routes: (*i*) tailoring their composition by tuning the enthalpy of mixing (ΔH_{mix}); (*ii*) rejuvenation of the amorphous structure via cryogenic thermal cycling [17,18] or various treatments [19–21]; and (*iii*) the formation of nanostructured MGs, such as amorphous nanogranular or columnar structures [22,23]. Among these, ΔH_{mix} is of particular importance, as its magnitude and sign dictate interatomic affinities, govern local order, and influence the thermodynamic stability of the amorphous phase [24]. Specifically, variations in ΔH_{mix} among constituent elements introduce competing thermodynamic driving forces that may, on the one hand, stabilize short-range order, while on the other, promote segregation or clustering of chemically incompatible elements [5]. This can lead to the development of atomic- and nano-scale heterogeneities through two thermodynamically distinct pathways: (*i*) nucleation and growth in the metastable regime, which requires overcoming an activation barrier and typically results in droplet-type morphologies, and (*ii*) spinodal decomposition in the unstable regime, where compositional fluctuations are amplified without a barrier, giving rise to interconnected morphologies [25]. For instance, nanoscale chemical heterogeneities of ~4-5 nm within the $Cu_{46}Zr_{37}Al_7Y_{10}$ MG facilitate the nucleation of multiple SBs and slow down their propagation, leading to more homogeneous plastic flow and improved plasticity [7]. In Al-Y-Ni MG, the nucleation and growth of uniformly dispersed fcc-Al particles (3-50 nm, depending on cooling rate) increases hardness and Young's modulus, while a particle volume fraction of ~10-20% maximizes fracture strength by impeding shear deformation [26]. In contrast, spinodal decomposition produces interconnected network-like morphologies, as reported for systems such as Pd-Si-Ag [27], Pd-Si-Au [28], Fe-B [29], Fe-Ni-B [30], and Zr-Ti-Cu-Ni-Be bulk metallic glasses (BMGs), where it precedes nanocrystallization [31]. In $Pd_{81}Si_{19}$ BMG, a fine network-like structure with a characteristic length of 3-6 nm formed by spinodal decomposition exhibits a large plastic engineering and true strain of 82 and 170%, respectively, in compression, together with initial strain hardening [32].

Alloying with immiscible elements provides a powerful route for stabilizing metastable amorphous phases and introducing nanoscale chemical heterogeneity in TFMGs. Previous studies on Nb-Cu [33,34], Ag-Ni [35], and Cu-Ta [36] amorphous films have shown that apparently uniform structure may contain spinodal-like fluctuations, nanoscale phase separation, or compositionally modulated amorphous regions. At the same time, ZrCuTi-Ta TFMGs [37] demonstrate that incorporation of an immiscible refractory element can enhance hardness and elastic modulus through changes in local bonding. Thus, immiscible alloying can tailor TFMGs by modifying the amorphous matrix and introducing chemical heterogeneities with different length scales, morphologies, and spatial distributions. However, the structural characteristics of such segregations and their role in controlling mechanical behavior of TFMGs remain insufficiently understood.

In the Zr-Cu-Fe system, ΔH_{mix} of the constituent pairs differs substantially. The Zr-Cu and Zr-Fe pairs exhibit strongly negative values of −23 and −22 kJ/mol, respectively [24], whereas the Cu-Fe pair displays a positive ΔH_{mix} of +12 kJ/mol [24]. The coexistence of these opposing interactions makes the Zr-Cu-Fe system a particularly attractive subject of investigation: whereas Zr-Cu and Zr-Fe bonding tendencies stabilize the amorphous phase, the unfavorable Cu-Fe affinity may promote phase separation. Several studies have addressed the atomic structure [38,39], glass-forming ability [40–42], and crystallization behavior of Zr-Cu-Fe MGs [43,44]. It was shown that minor Fe additions (2.5-12.5 at.%) to $Cu_{50}Zr_{50}$ BMG enhance glass-forming ability and stabilize the B2-CuZr phase [44]. Structural studies on $Zr_{60}Cu_{20}Fe_{20}$ reveal shortened Zr-Cu and Zr-Fe bonds and a more densely packed amorphous structure, with Cu and Fe uniformly distributed on the medium-range scale [38,43]. At higher Fe contents, rapid solidification induces liquid-liquid phase separation, forming a Fe-rich glassy matrix homogeneously embedded with nanoscale (2-8 nm) Cu-rich particles [39]. At intermediate concentrations of Fe (x = 0.45-0.5) in $(Cu_{1-x}Fe_x)_{90}Zr_{10}$, solidification induces spinodal decomposition, yielding a two-phase interconnected structure, where the solute element Zr dissolves in both Cu-rich and Fe-rich regions. In contrast, at higher Fe concentrations (x = 0.6), particle-isolated structures formed by nucleation and growth [39]. Such enthalpy-driven heterogeneities are expected to govern the nucleation and propagation of SBs, thereby affecting the mechanical behavior. However, the mechanical properties of Zr-Cu-Fe MGs remain largely unexplored, and studies on TFMGs are entirely lacking.

In the present work, Zr-Cu-Fe TFMGs are employed as a model system to investigate how compositional variation governs nanoscale heterogeneity and its impact on structural and mechanical behavior. Guided by thermodynamic modeling, which predicts amorphous structure up to 77.5 at.% Fe, we provide a holistic investigation combining structural, mechanical, and computational characterization across both ZrCu-rich and Fe-rich compositions, extending beyond previous studies [38–44] limited to single compositions or minor Fe concentrations. Among the main results, we observe an enrichment in the fraction of densely packed icosahedral configurations at Fe concentration of 17-29 at.%, whereas structural disorder accompanied by increased fraction of unfavorable motifs occurs when Fe concentration is > 54 at.%. Atom probe tomography further reveals the formation of nanoscale amorphous Cu-rich clusters at 76 at.% Fe. The appearance of these nanoscale chemical heterogeneities correlates with the suppression of shear localization during nanoindentation, leading to reduced serration amplitude from 16.2 to 5.4 and a more homogeneous plastic flow. All these findings demonstrate how controlled nanoscale heterogeneities can be used to tailor the mechanical behavior of TFMGs, which can be extended to other MG families. Moreover, these insights are important for advancing the scalability of findings to bulk MG counterparts and for guiding the design of nanoengineered TFMGs tailored for various applications.

2. Materials and methods

2.1. Thermodynamic calculation

The glass-forming compositional range in the Zr-Cu-Fe system was evaluated based on thermodynamic stability criteria, in which the formation of the amorphous phase is favored when its free energy (ΔG_{am}) is lower than that of the corresponding crystalline solid solution (ΔG_{ss}) at a given temperature [45]. ΔG_{am} can be defined as:

$$\Delta G_{am} = \Delta H_{am} - T\Delta S_{am} \quad (1)$$

while ΔG_{ss} can be expressed as:

$$\Delta G_{ss} = \Delta H_{ss} - T\Delta S_{ss} \quad (2)$$

where ΔH_{am}, ΔH_{ss}, and ΔS_{am}, ΔS_{ss} are the enthalpies and entropies of mixing for the amorphous phase and solid solution, respectively, and T is the temperature (298 K).

The ΔH_{am} and ΔH_{ss} were evaluated using the semi-empirical model proposed by Van der Kolk et al. [46], which takes pure crystalline elements as a common reference. ΔH_{am} consists of a chemical contribution (determined by mixing enthalpies $\Delta H_{i,j}^{mix}$ between elements i and j) and a topological disorder term (under the assumption that the enthalpy of the amorphous pure metals is equivalent to that of the corresponding liquid metals $T_m\Delta S_m$). The chemical contribution is derived from binary mixing enthalpies: −23, −22, and +12 kJ/mol for Zr-Cu, Fe-Zr, and Cu-Fe pairs

[24], respectively. The topological disorder term approximates the enthalpy of amorphous pure metals by that of their corresponding liquids. According to Van der Kolk et al., melting entropy ΔS_m can be replaced by a reduced liquid entropic term $\alpha = 3.5\ J \times mol^{-1} \times K^{-1}$ [47].

2.2. Ab initio molecular dynamics (AIMD) simulations and atomic cluster analysis

AIMD simulations were employed to model the amorphous structure with different Fe content. The simulations were conducted using the Vienna Ab initio Simulation Package (VASP) [48]. Model systems consisting of 256 atoms of $(Zr_{34}Cu_{66})_{100-x}Fe_x$ (x = 0, 6, 11, 17, 22, 29, 54, and 76 at.%) were constructed within parallelepiped-shaped simulation cells under periodic boundary conditions. To obtain a uniformly disordered melt, each alloy was initially melted at 2500 K and equilibrated at this temperature for at least 11 ps under an isothermal-isobaric (NPT) ensemble. Subsequently, the systems were continuously quenched to 300 K at a cooling rate of 7.33×10^{15} K/s, corresponding to a timestep of 0.3 fs over 1000 steps, and then relaxed at 300 K. The structural properties were then calculated by performing the statistical averages over 600 molecular-dynamics steps of the quenched structures. The atomic configurations were analyzed using Voronoi tessellation with the OVITO software package [49].

2.3. Thin films synthesis

$(Zr_{34}Cu_{66})_{100-x}Fe_x$ TFMGs have been deposited by co-sputtering from $Zr_{40}Cu_{60}$ (at.%) and pure Fe targets using radio frequency (RF) magnetron sputtering. The magnetron sputtering system was used with a fixed distance between the targets and the substrate equal to 100 mm and the targets tilted at 20°. Background pressure $<5.0 \times 10^{-6}$ Pa was reached before the deposition. Sputtering was performed at room temperature with a substrate rotation velocity of 10 rpm. A constant Ar flow rate of 40 sccm has been used, resulting in a working pressure of 3×10^{-1} Pa. The regulation of power applied to targets, ranging from 13 to 123 W, allowed fine control of the film composition. A detailed description of the power combinations used is provided in the Supplementary Information, Table S1.

Si (100) + 300 nm thick SiO_2 substrates were used for scanning and transmission electron microscopy (S/TEM), X-ray diffraction (XRD), nanoindentation, and Brillouin light scattering (BLS). Kapton® substrates were used for tensile testing, including *in situ* measurements of electrical resistance. In all cases, the film thickness was equal to ~800 nm. Microtip coupons from Cameca were coated with ~500 nm thick films for atom probe tomography (APT) measurements. Film thickness was determined using a Veeco Dektak 6M profilometer.

2.4. Structural characterization

A scanning electron microscope (SEM) LEO 1530 Carl Zeiss AG, equipped with an energy dispersive X-ray spectroscopy (EDX) detector (Oxford Instruments), was used to perform morphological and chemical composition characterization of samples.

Grazing incidence X-ray diffraction (GI-XRD) and X-ray Reflectivity (XRR) measurements were carried out with an Empyrean series 3 diffractometer (Malvern Panalytical) using Cu-Kα radiation (λ = 0.154 nm) at 40 kV and 40 mA. GI-XRD measurements were performed at grazing angle of 1° in continuous scan mode within the 2θ range 20-60° with a step size of 0.02° and time per step of 7 s. XRR measurements were carried out in continuous scan mode for the range of 0.1-1° with a step size of 0.005° and time per step of 1 s.

Conventional and high-resolution TEM measurements were carried out using Thermo Fisher Themis-Z at 300 kV with a double aberration corrector. TEM lamellae were prepared using a FEI Strata 400 Ga focused ion beam (FIB) following the procedure described elsewhere [50].

Microtips have been sharpened prior to APT analyses using a Zeiss Auriga 60 Dual Beam FIB. APT experiments were performed in a LEAP 4000X HR (Cameca Instruments, Madison, WI, USA) in pulsed voltage mode with a pulse fraction of 20% and frequency of 100 kHz. The base temperature of the sample was kept at 40 K, with the detection rate set to 0.005 ions per pulse. Data reconstruction and analysis were done using the software package AP Suite 6.3.1 (Cameca Instruments). A nearest-neighbor distance (NND) analysis [51,52] was conducted to further evaluate potential chemical heterogeneities.

2.5. Mechanical characterization

Tensile tests were performed on TFMGs deposited on flexible Kapton® substrates, with dimensions of 40 x 1.5 × 0.18 mm (length x width x thickness), using a 300 N Deben tensile machine combined with a Keyence VHX optical microscope. The tensile speed and the gage length were, respectively, equal to 8.3×10^{-3} mm/s and 25.4 mm, corresponding to an initial strain rate of $\sim 3.3 \times 10^{-4}\ s^{-1}$. 200× magnification was used to visualize a sufficient number of cracks and to determine their linear density (orthogonal to the loading direction). Further details can be found elsewhere [53].

Five samples for each state were measured to determine the crack onset strain (COS) and the evolution of the linear crack density. During the tensile tests, the electrical resistance was measured using a Keithley 2400 SourceMeter. Specifically, we exploited the methodology of N. Lu, X. Wang, and J. Vlassak [54], estimating the COS when the change in the resistance is 15% [55] above the constant volume approximation, as described:

$$\frac{R}{R_0} = \frac{L}{L_0} = (1+\varepsilon)^2 \tag{3}$$

where R is the electrical resistance of the film stretched to the gage length L, R_0 is the initial resistance before deformation, and ε is the strain.

Brillouin light scattering (BLS) experiments were performed to extract the elastic constants of TFMGs. Measurements have been carried out in standard backscattering geometry for opaque materials, with an incident laser beam (single-mode solid-state laser Torus, Quantel) wavelength of $\lambda_L = 532$ nm. TFMGs are considered isotropic with two independent elastic constants, C_{11} and C_{44}, from which the Young's modulus (E) can be calculated. More details can be found in Ref. [56].

Nanoindentation tests were performed using a FemtoTools FT-NMT04 nanoindenter with an FT-S20′000 Berkovich diamond tip, with a maximum force range of 20 mN and a resolution of 0.05 μN. The area function of the tip was calibrated using a standard fused silica reference sample using the Oliver and Pharr method [57]. Continuous stiffness measurements (CSM) were performed at 200 Hz and 2 nm amplitude in displacement control mode at strain rates equal to 0.1, 0.5, and 1 s^{-1}. A minimum of 10 indentations were performed on each sample. The E and hardness (H) were extracted at indentation depth ranging from 70 to 90 nm, corresponding to ~10% of the thickness. The strain rate sensitivity (m) was determined as the slope of fitting curves of H at different strain rates. The activation volume (V) was estimated based on the model of W. Johnson and K. Samwer [58] using the following equation:

$$V = \frac{3\sqrt{3}\,k\,T}{m\,H} \tag{4}$$

where k is the Boltzmann constant and T is the temperature.

Nanoindentation tests in force control mode at constant loading rates of 0.5 and 5 mN/s were performed to study the serrated flow of TFMGs. The indentation strain rate was calculated as:

$$\dot{\varepsilon}_i = \frac{1}{h} * \frac{dh}{dt} \tag{5}$$

where h is the displacement and t is the time. When $\dot{\varepsilon}_i$ is plotted as a function of depth, discrete pop-in events manifest as sharp peaks. The serration analysis was carried out in the penetration-depth range of 100-300 nm. The prominence of serrated flow can be quantified using the non-dimensional height, A, of these peaks:

$$A = \frac{\dot{\varepsilon}_i^{max}}{\dot{\varepsilon}_i^{base}} \quad (6)$$

where $\dot{\varepsilon}_i^{max}$ and $\dot{\varepsilon}_i^{base}$ represent the maximum and baseline strain rates, respectively [59].

3. Results

3.1. Thermodynamic landscape of the Zr-Cu-Fe system: evaluation of glass-forming range and AIMD analysis

3.1.1. Alloy selection: tailoring mixing enthalpy in $(ZrCu)_{100-x}Fe_x$ TFMGs

To systematically explore how compositional tuning affects the formation of heterogeneities and their impact on mechanical behavior, we first evaluated the glass-forming range of the Zr-Cu-Fe system. Specifically, glass-forming ability was used as an indicator of the relative stability of different compositions. By deliberately varying the alloy chemistry, our aim was to destabilize the amorphous phase in a controlled manner, thereby promoting the formation of local chemical fluctuations.

The glass-forming compositional range in the Zr-Cu-Fe system was evaluated based on thermodynamic stability criteria and shown in Fig. 1a. The compositional domain aligns well with the glass-forming range reported in Ref. [40]. According to the Miedema's model explained above, keeping the fixed ratio of Zr to Cu equal to 1:2, corresponding to a base composition $Zr_{34}Cu_{66}$, the amorphous phase is predicted to be stable up to 77.5 at.% Fe, beyond which crystallization becomes thermodynamically preferred (Fig. 1a).

Fig. 1b shows that the value ΔG_{am} - ΔG_{ss} increases with Fe content. Positive values of this difference indicate a lower relative thermodynamic stability of the amorphous phase compared to the competing crystalline solid-solution state. The observed compositional dependence therefore suggests that increasing Fe content progressively destabilizes the amorphous phase and enhances the tendency for chemical segregation or crystallization (Fig. 1b).

This effect was intentionally employed in the present work as a design parameter to tailor chemical segregation and microstructural heterogeneity in the Zr-Cu-Fe system. For these reasons, we synthesized a series of TFMGs with composition $(Zr_{34}Cu_{66})_{100-x}Fe_x$, varying the Fe content from 0 up to 76 at.% (0, 6, 11, 17, 22, 29, 54, and 76 at.%).

3.1.2. Structural modeling using AIMD

AIMD simulations have been employed as a predictive tool to evaluate the amorphous phase formation, identify dominant local atomic motifs, and examine the structural heterogeneity as a function of Fe content.

The shape of atomic pair correlation functions ($G(r)$) curves for $(Zr_{34}Cu_{66})_{100-x}Fe_x$ TFMGs (Fig. 2a) are in line with those reported for ZrCu system in earlier papers [60–62]. The peak positions are shifted towards lower nearest neighbor distance (r) values, and the shape of the first and second maxima are altered, varying the Fe concentration. Specifically, low Fe-content TFMGs (up to 22 at.%) exhibit two components of the first maximum, corresponding to longer (Zr-Zr) and shorter (Zr-Cu, Cu-Cu, Cu-Fe, and Fe-Fe) distances within the first coordination shell (Table S2). As the Fe content increases, the proportion of longer interatomic bonds decreases, leading to lower distances, indicating atomic densification with Fe enrichment.

For all compositions, the second peak of $G(r)$ exhibits splitting, which is attributed to distinct cluster connectivity modes between short-range ordered motifs in MGs, namely vertex-, edge-, and face-sharing, resulting in a bimodal distribution of second-nearest neighbor distances [63].

The distributions of the average coordination number (CN), as well as the CNs of individual species (Cu, Zr, and Fe), are reported in Fig. 2b and Fig. S1, respectively. At low Fe concentrations, the system exhibits a clear bimodal CN distribution, with two distinct peaks centered around CN ~12 and ~16, corresponding to the characteristic local environments of Cu and Zr atoms [62,64], respectively. As the Fe content increases to ~22-29 at.%, the peak at CN ~16 diminishes into a weaker shoulder and the overall distribution broadens. Similar trends have been reported for MGs, where alloying elements disrupt bimodal coordination distribution and enhance structural heterogeneity, ultimately influencing the glass forming ability [64].

To further elucidate the local topological order, we carried out a Voronoi tessellation analysis (Fig. 2c and d), which is widely employed to investigate the characteristics of the local order [65]. The Voronoi polyhedral index is usually expressed as $< n_3, n_4, n_5, n_6 >$, where n_i denotes the number of i-edged faces of the Voronoi polyhedra [49].

Firstly, we observed that the Zr-centered local environment in the ZrCu system shows no dominant structural motif, and the most common Zr-centered polyhedra have lower fractions (less than 2% of the total number of polyhedra) [66,67]. Moreover, their population shows only a weak dependence on the composition, with only gradual shifts primarily associated with changes in coordination number; therefore, we focused the analysis on Cu-centered and Fe-centered polyhedra. Fig. 2c shows the concentration evolution of the five most prevalent Cu-centered polyhedra present in ZrCu-based MGs, namely <0,0,12,0>, <0,2,8,

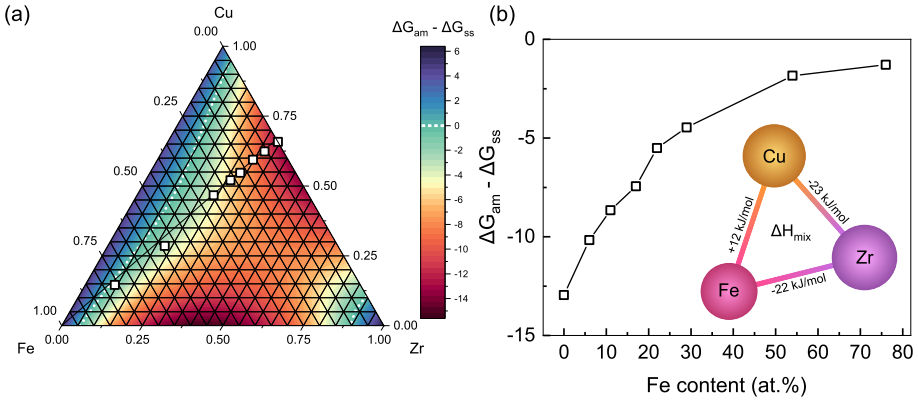

Fig. 1. Thermodynamic landscape of the Zr-Cu-Fe system. (a) 2D maps of Gibbs free energy for the Zr-Cu-Fe system. An amorphous structure is expected for compositions exhibiting a negative difference between ΔG_{am} and ΔG_{ss} (region between the two dashed white lines). The thin black line represents the compositions of Zr-Cu-Fe with a constant 1:2 ratio Zr:Cu. White squares highlight the compositions synthesized in this work. (b) Difference between ΔG_{am} and ΔG_{ss} as a function of the Fe content in $(Zr_{34}Cu_{66})_{100-x}Fe_x$. The inset shows ΔH_{mix} between Zr, Cu and Fe, with their relative atomic size differences represented by spheres.

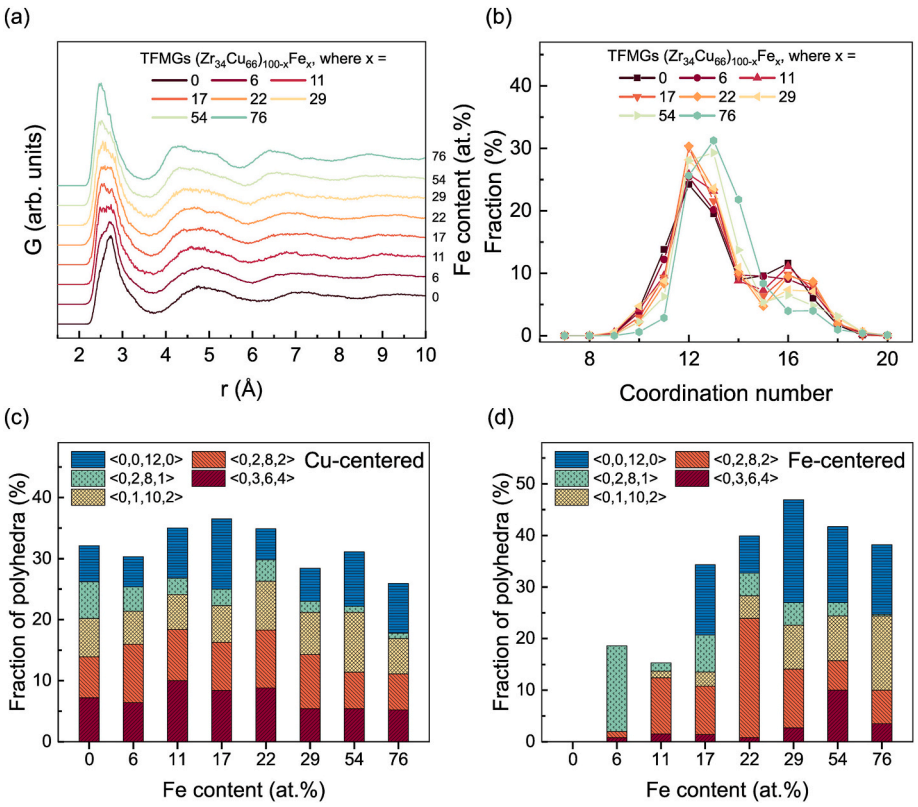

Fig. 2. Structural modeling using *ab initio* MD simulations. (a) PDF for $(Zr_{34}Cu_{66})_{100-x}Fe_x$ TFMGs with various Fe content. (b) Distribution of average coordination numbers. (c, d) Fraction of Cu- and Fe-centered polyhedra.

1>, <0,2,8,2>, <0,1,10,2>, and <0,3,6,4>. The fraction of ideal icosahedra <0,0,12,0> is lower than values reported in prior studies, while the fractions of the other dominant polyhedra are in good agreement with the values reported in the literature for $Zr_{34}Cu_{66}$ MG [61,62]. This reduction is attributed to the pronounced sensitivity of <0,0,12,0> polyhedra to the quenching rate [62,68]. Specifically, the high cooling rate employed in the simulation (7.33×10^{15} K/s) hinders the formation of such perfect icosahedra, compared to classical MD simulations or experimental studies conducted at lower cooling rates. This trend is further supported by additional simulations performed at a lower cooling rate of 7.33×10^{12} K/s (Tables S3 and 4).

As the Fe content increases, the fraction of Cu-centered <0,0,12,0> polyhedra initially increases, reaching a maximum of 11.5% at 17 at.% Fe (Fig. 2c). This is followed by a moderate decline in their population down to 5.1%, with a subsequent increase up to 8.1% observed at higher Fe concentrations of 54 and 76 at.%. A similar trend is also observed for the fraction of high-population polyhedra, with an initial increase up to 17-22 at.% Fe, followed by a decrease at higher Fe concentrations.

The structural role of Fe-centered polyhedra progressively increases with higher Fe concentrations, as shown in Fig. 2d. At low Fe concentrations (6-11 at.%), the overall population of Fe-centered clusters remains relatively low and dominated by polyhedra such as <0,2,8,2>, <0,2,8,1>, and <0,3,6,4>. The prevalence of polyhedra such as <0,2,8,2>, <0,2,8,1> indicates a relatively disordered local environment, characteristic of a chemically heterogeneous structure with weak short-range order. These polyhedra are among the more frequently observed "disordered" motifs in Fe-based MGs and typically do not provide dense atomic packing, which may correspond to an atomic structure with increased free volume [69].

As the Fe content further increases (17-29 at.%, Fig. 2d), the fraction of Fe-centered polyhedra grows markedly, with <0,0,12,0> icosahedra becoming dominant. In addition, the fraction of <0,1,10,2> polyhedra increases in agreement with AIMD simulations carried out in Ref. [70]. The presence of these motifs suggests an enhanced short-range topological order and potentially increasing the stiffness of the material [70,71]. With further increase in Fe, the fraction of <0,0,12,0> polyhedra slightly decreases (Fig. 2d), while the population of <0,1,10,2> polyhedra continues to grow, reaching its maximum at 76 at.% Fe. At the Fe concentrations of 54 and 76 at.%, a slight decrease in the total fraction of these most prevalent Fe-centered polyhedra is observed.

3.2. Structural characterization

3.2.1. Structural characterization of $(ZrCu)_{100-x}Fe_x$ TFMGs

Fig. 3 shows cross-section SEM images of different $(Zr_{34}Cu_{66})_{100-x}Fe_x$, reporting a network of fine corrugation patterns, indicative of their amorphous nature. Specifically, corrugations are likely associated with localized regions that accommodate plastic deformation preferentially during mechanical loading (e.g., fracture). Similar patterns have been reported in various BMGs and ZrCu TFMGs [72].

Fig. 4a shows the XRD patterns of all compositions, reporting the presence of a broad diffuse hump, characteristic of an amorphous structure, while the pure Fe film displays a BCC crystalline structure. With increasing Fe content, the position of the amorphous hump linearly shifts towards higher 2θ angles, converging to the position of the crystalline Fe (110) peak (Fig. 4b). This trend, consistent with AIMD simulations (Fig. 2a), reflects a reduction in the average interatomic spacing, which can be estimated using the Ehrenfest equation [73]. As the Fe content increases from 0 to 76 at.%, the spacing decreases from ~2.71 down to 2.54 Å, driven by the progressive substitution with Fe atoms, which have a smaller atomic radius (126 p.m. vs 128 p.m. and 160 p.m. for Cu and Zr, respectively), as shown in Fig. 4c. Moreover, Fig. 4b illustrates the compositional dependence of the full width at half maximum (FWHM), which decreases from 7.25 down to 4.57° as the Fe content increases up to 76 at.%, and further decreases to 0.52° for crystalline Fe. Fig. 4d shows that with increasing the Fe content, the

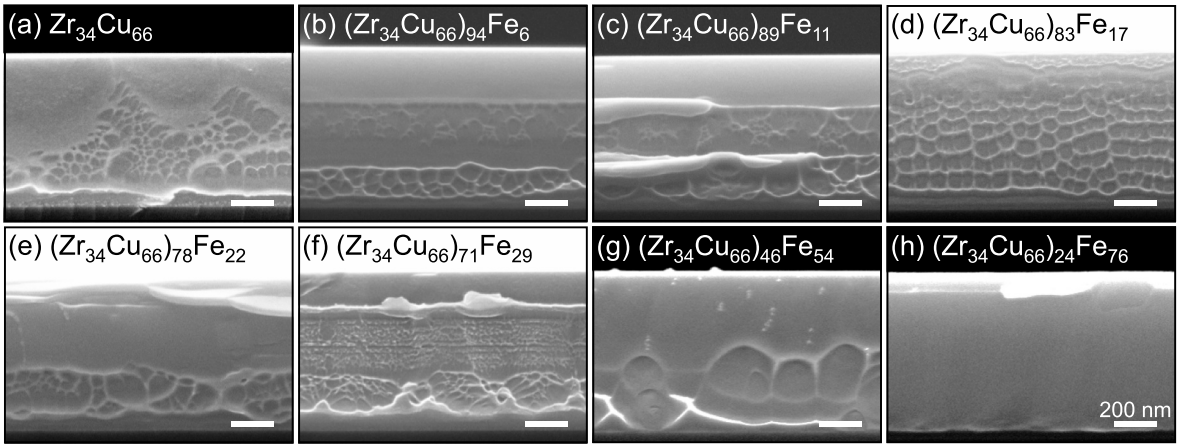

Fig. 3. SEM characterization. Cross-section SEM images displaying the morphology of $(Zr_{34}Cu_{66})_{100-x}Fe_x$ TFMGs with Fe content from 0 up to 76 at.% (a-h).

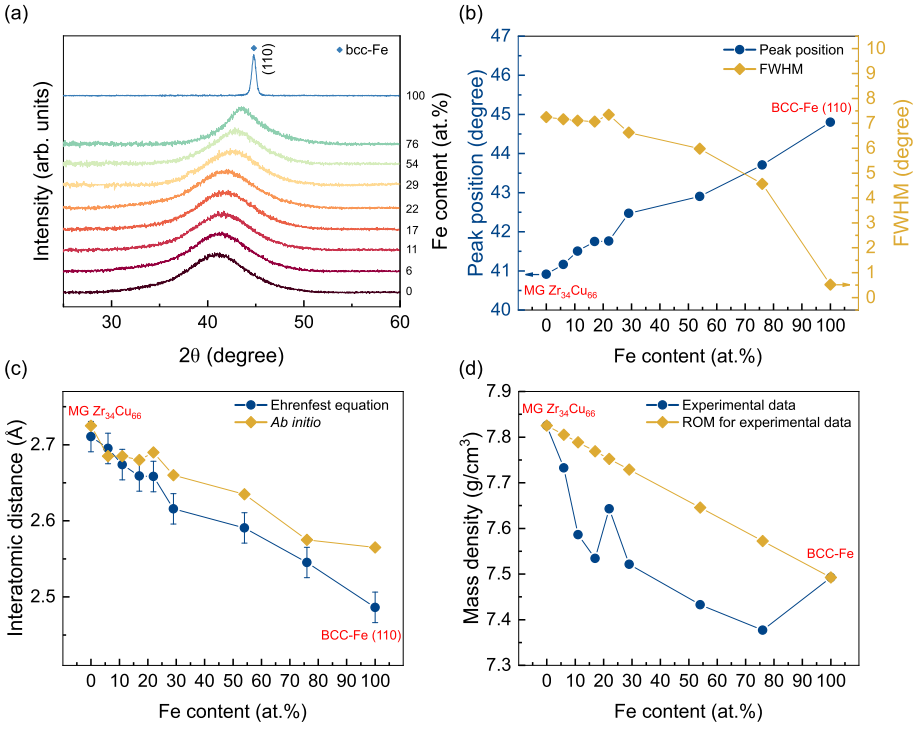

Fig. 4. XRD characterization. (a) XRD diffractograms of different $(Zr_{34}Cu_{66})_{100-x}Fe_x$ TFMGs. (b) Evolution of the amorphous peak position and FWHM with increasing Fe concentration. (c) Average interatomic distances estimated using the Ehrenfest equation and AIMD simulations. (d) Mass density compared with the rule of mixtures.

mass density gradually decreases from 7.82 down to 7.57 g/cm^3, in agreement with AIMD simulations and the rule of mixtures (ROM), reflecting the substitution of heavier Cu and Zr atoms with lighter Fe atoms. The deviation from the ROM stems mainly from the fact that it is calculated based on the density of crystalline Fe.

TEM and high-resolution transmission electron microscopy (HRTEM) observations were performed to assess the microstructural homogeneity of representative alloys with 6 and 76 at.% Fe (Fig. 5). The selected area electron diffraction (SAED) patterns (insets in Fig. 5a–c) shows broad diffuse rings, confirming a fully amorphous structure consistent with XRD results (Fig. 4). TEM images and EDX maps (Fig. 5a–d) had not revealed any nanocrystallization, phase separation, or chemical segregation, indicating a spatially uniform distribution of Zr, Cu, and Fe even at high Fe content.

3.2.2. *Characterization of nanoscale heterogeneities*

To overcome TEM limitations in terms of the lamella thickness and limited EDX spatial resolution [34] and to obtain atomic-scale insight into the local chemical environment, we carried out APT experiments, offering three-dimensional elemental mapping with sub-nanometer spatial resolution and high chemical sensitivity [74].

Fig. 6a presents a reconstructed volume with 64.5 at.% Cu iso-compositional surfaces for the $Zr_{34}Cu_{66}$ TFMG. No apparent elemental segregation is observed, while the corresponding concentration profiles confirm a homogeneous distribution of elements (Fig. 6c). The measured concentrations of Cu and Zr are in close agreement with those obtained from EDX analysis. However, due to the limited discernability of the visual representation given by the point clouds, NND analysis [51,52] was conducted to further evaluate potential chemical heterogeneities. Experimental distributions of the 3rd order nearest-neighbor distances (count) between Cu atoms were compared with those expected from a

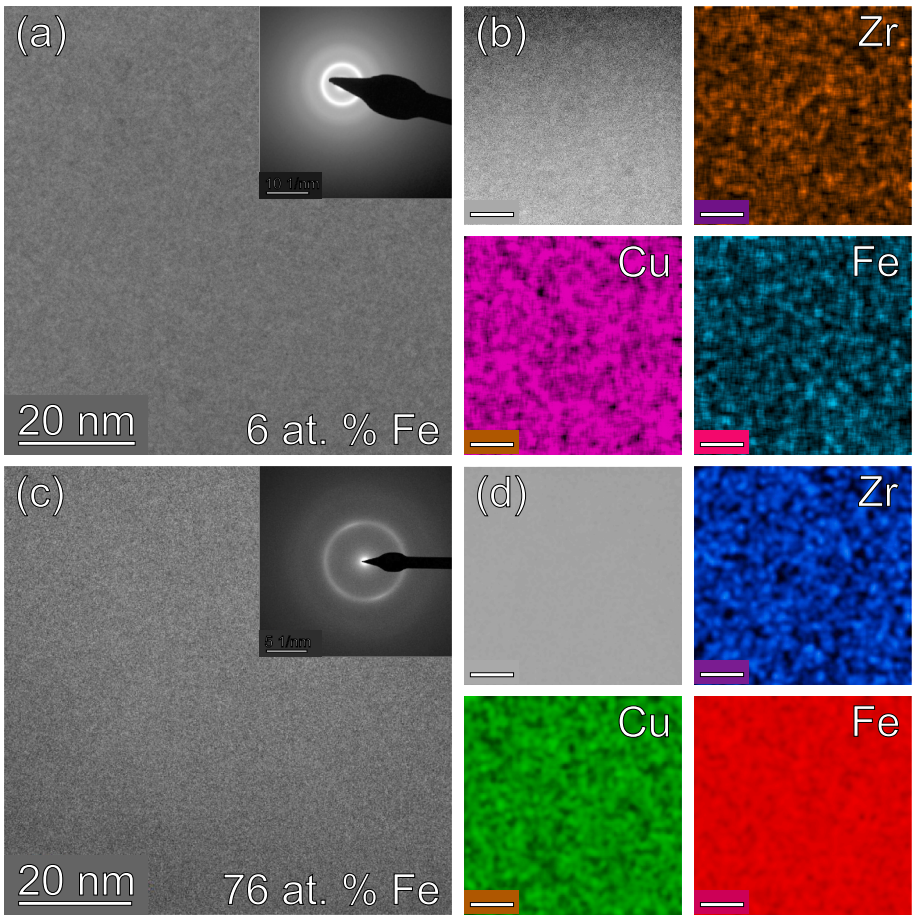

Fig. 5. Microstructural characterization. TEM and corresponding HAADF STEM images with elemental distribution maps of $(Zr_{34}Cu_{66})_{100-x}Fe_x$ TFMGs with Fe content of: (a, b) 6 at.%; (c, d) 76 at.%. Scale bars are 10 nm.

random distribution of solute atoms, based on APT analysis (randomized count). No significant deviation from the randomized distribution was found, indicating that Cu atoms are homogeneously distributed (Fig. 6e). This supports the homogeneous nature of $Zr_{34}Cu_{66}$ in agreement with TEM (Fig. 5a and b) and XRD (Fig. 4) results.

Fig. 6b shows the reconstructed volume obtained from the APT data, illustrating iso-compositional surfaces of 33 at.% Cu for the $(Zr_{34}Cu_{66})_{24}Fe_{76}$ TFMG. The reconstruction reveals a chemically homogeneous matrix containing nanoscale Cu-rich clusters with sized of several nanometers. Composition profiles (Fig. 6d) extracted from regions containing these clusters confirm their Cu enrichment, accompanied by a depletion of Fe and Zr. The experimental distribution of the 3rd order NND (Fig. 6f) deviates significantly from those expected for a random distribution, indicating the presence of Cu atom clustering within the matrix in agreement with the APT reconstruction (Fig. 6b).

3.3. Mechanical characterization

3.3.1. Evolution of hardness, Young's modulus, and fracture

Fig. 7a reports the crack density evolution during tensile testing of TFMGs deposited on a flexible substrate. The inset indicates the apparition of the first crack, also referred to as the crack onset. As the Fe content increases from 0 to 54 at.%, the COS decreases progressively from ~2.2 down to ~1.6%, while a further increase in Fe content up to 76 at.% leads to its increment up to ~2%. After the onset of cracking, the deformation is characterized by a rapid accumulation of cracks across all compositions (Fig. 7a). The crack density increases rapidly with strain until a saturation regime is reached, beyond which no additional cracks are formed [75]. The highest crack density was observed for the samples containing 0 and 29 at.% Fe, whereas the film with the highest Fe content (76 at.%) shows the lowest crack density. Measurements of normalized electrical resistance reveal a similar trend of the COS variation with Fe content, as shown in Fig. 7b.

Fig. 7c shows that the E measured by nanoindentation and BLS of the $(Zr_{34}Cu_{66})_{100-x}Fe_x$ TFMGs increases at larger Fe contents. Specifically, the values of E determined by BLS are in the range from ~101.9 to ~116.3 GPa, while those obtained by nanoindentation oscillate between ~119.2 and ~139.2 GPa in good agreement with E values reported in the literature for ZrCu MGs [76–78]. The increment in E is attributed to progressive densification of atomic packing and formation of shorter, stronger interatomic bonds with increasing Fe content [77,79] in agreement with the AIMD simulations (Fig. 2a) and with XRD results (Fig. 4b). Furthermore, this trend is expected as Fe-based MGs exhibit higher E compared to Cu- and Zr-based MGs [80].

The H of the $Zr_{34}Cu_{66}$ TFMG is ~7.9 GPa (Fig. 7d), which is consistent with previously reported values for this composition [78,79]. Upon increasing the Fe content, H increases, reaching a maximum of ~8.5 GPa (Fig. 7d) at 29 at.% Fe, beyond which it progressively decreases down to ~7.65 GPa at 76 at.% Fe. Values of E and H measured at strain rates of 0.1, 0.5, and 1 s^{-1} are shown in Fig. S2.

Fig. 7e demonstrates that all studied compositions follow a consistent trend in strain-rate sensitivity (m), showing an increase in H with increasing strain rate. Moreover, Fig. 7f reveals that m has compositional dependence, evolving from ~0.033 for the $Zr_{34}Cu_{66}$ TFMGs, (in good agreement with values previously reported for ZrCu and ZrCu-based TFMGs [81–83]) up to a maximum value of ~0.052 at 29 at.% Fe, after which it decreases down to ~0.029 at 76 at.% Fe.

The trend of activation volume (V) as a function of the Fe content is

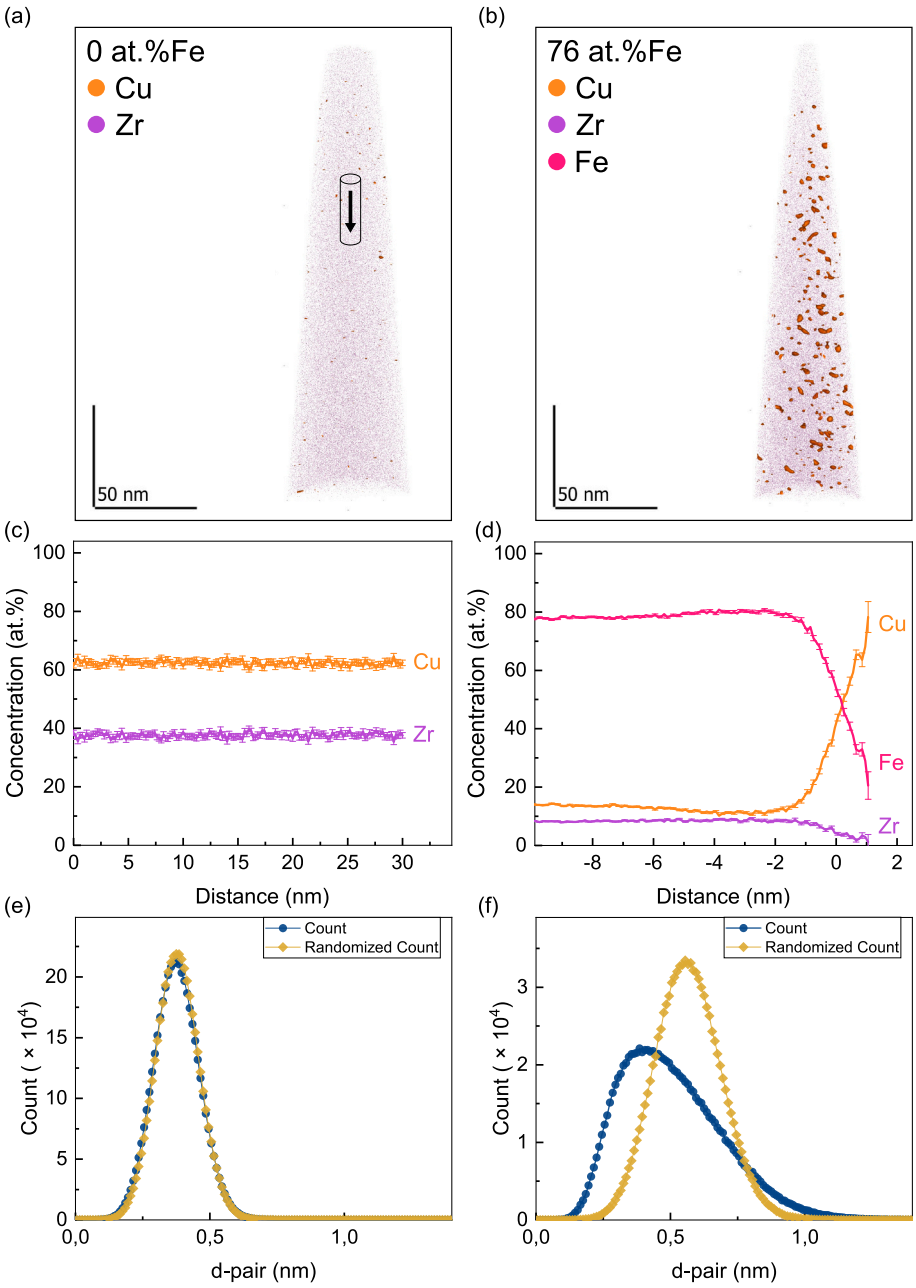

Fig. 6. APT reconstruction and NND analysis. (a, b) 3D reconstructed volume of a tip visualized using iso-compositional surfaces of 64.5 and 33 at.% Cu for $Zr_{34}Cu_{66}$ and $(Zr_{34}Cu_{66})_{24}Fe_{76}$, respectively. (c) Concentration profiles extracted from the cylinder in $Zr_{34}Cu_{66}$. (d) Concentration profiles in the form of a proximity histogram for ten largest clusters (based on the isosurface) in $(Zr_{34}Cu_{66})_{24}Fe_{76}$. (e, f) 3rd order NND distributions of Cu-Cu in $Zr_{34}Cu_{66}$ and $(Zr_{34}Cu_{66})_{24}Fe_{76}$, respectively.

reported in Fig. 7f. For the $Zr_{44}Cu_{66}$ TFMGs, V is ~78.4 Å^3, it decreases gradually to ~47.3 Å^3 at 29 at.% Fe and subsequently increases up to ~92.3 Å^3 at 76 at.% Fe. The observed increase in activation volume at higher Fe concentrations may indicate the formation of larger shear transformation zones (STZs), potentially originating from Fe-induced structural heterogeneities.

3.3.2. *Serrated flow and localized deformation behavior*

To further elucidate the effect of Fe addition and the associated structural heterogeneities on the SBs activity, a detailed analysis of pop-in events during nanoindentation loading was conducted.

The indentation strain rate was plotted as a function of indentation depth for each loading rate (Fig. S3). These curves contain serrations, which are indicative of localized deformation and SBs activity. The amplitude of each such burst was quantified as a measure of strain localization (Fig. 8a). Slower loading rate (0.5 mN/s) allows SBs to nucleate and propagate more extensively, resulting in larger pop-ins, while higher loading rate (5 mN/s) suppress the development of large serrations as the imposed deformation rate exceeds the inherent sliding speed of SBs [1,3].

At low loading rate, the serration amplitude remains nearly constant up to ~29 at.% Fe and decreases markedly only at higher Fe content, from ~16.2 down to 5.4 at 76 at.% Fe (Fig. 8b). This indicates that shear localization is suppressed in the Fe-rich states, where chemical heterogeneities may lead to a dissipation of a single dominant SB into numerous small and spatially distributed shear events (Fig. 8c).

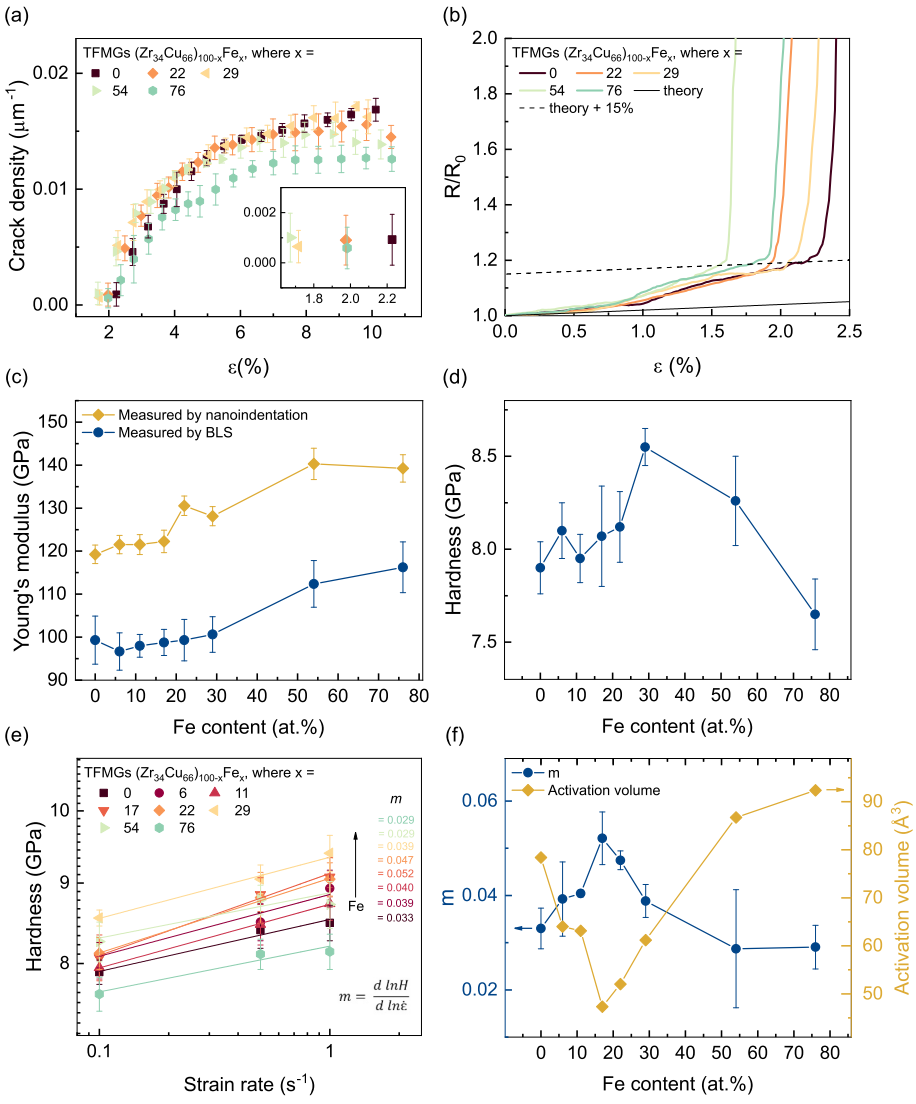

Fig. 7. Mechanical behavior. (a) Crack density and (b) change in normalized electrical resistance, R/R_0, as a function of strain for $(Zr_{34}Cu_{66})_{100-x}Fe_x$ TFMGs. The inset shows the magnified region of the COS. (c) Values of E and (d) H measured at strain rate of 0.1 s^{-1}. (e) Evolution of H as a function of different strain rates with the strain rate sensitivity (m) values indicated on the right-hand side. (f) Dependence of strain rate sensitivity values and activation volume on Fe content.

4. Discussion

4.1. Evolution of the atomic structure

The investigated TFMGs remain fully amorphous across the entire composition range (0 - 76 at.%). However, the addition of Fe induces notable changes in short- and medium-range order. The shift of the first-neighbor peak in $G(r)$ to lower r with increasing Fe (Fig. 2a) indicates reduced interatomic spacing and denser atomic packing. XRD confirms this trend, showing the amorphous hump shifting to higher angles (Fig. 4a), with a narrower FWHM decreasing from 7.25 to 4.57°, reflecting increased local order and the interatomic distance approaching that of crystalline Fe. As reported for CuZr-Nb alloys [84], alloying with small atoms shorten bonds and enhance packing efficiency in MGs. In a similar way, in the Zr-Cu-Fe system, the substitution of larger Zr/Cu atoms by smaller Fe atoms also reduces interatomic distances. Thermodynamic modeling (Fig. 1b) reveals that the tendency to crystallization increases with the Fe concentration, indicating reduced thermodynamic stability of the amorphous phase and a greater tendency of disordered structure for structural rearrangements. This is also supported by ΔH_{mix} of the Cu-Fe pair [24], which destabilizes the amorphous structure at high Fe content.

To further clarify the structural evolution, coordination number distributions were analyzed. The analysis shows that $Zr_{34}Cu_{66}$ exhibits a bimodal CN distribution (with maxima at, respectively, ~12 for Cu-centered and at ~16 for Zr-centered clusters (Fig. 2b). This behavior is consistent with previously reported CN distributions for Cu and Zr in binary ZrCu MGs [62,64]. Fe addition gradually suppresses the peak at CN ~16, shifting the distribution toward a unimodal shape centered at CN ~13. This reflects the breakup of large Zr-centered clusters, increased prevalence of Fe- and Cu-centered motifs, and a structure with predominantly intermediate coordination numbers, consistent with trends reported for other MGs [85].

Voronoi analysis provides deeper insight into the local motifs underlying structural changes. The Cu-centered <0,0,12,0> icosahedron is the dominant structural motif stabilizing ZrCu MGs [86] and Fe additions (≤17 at.%) nearly double their population (Fig. 2c). Upon that, the number of Fe-centered icosahedra increases as well (Fig. 2d). This agrees with literature showing that small ternary additions enhance icosahedral ordering by promoting energetically favorable 12-fold packing [85]. In our work, this tendency is observed at low Fe concentrations of 17-29 at.%, where substantial fraction of Fe atoms adopts <0,0,12,0> motif. However, beyond ~29 at.% the fraction of <0,0,12,0> icosahedra decreases which are replaced by distorted motifs such as <0,1,

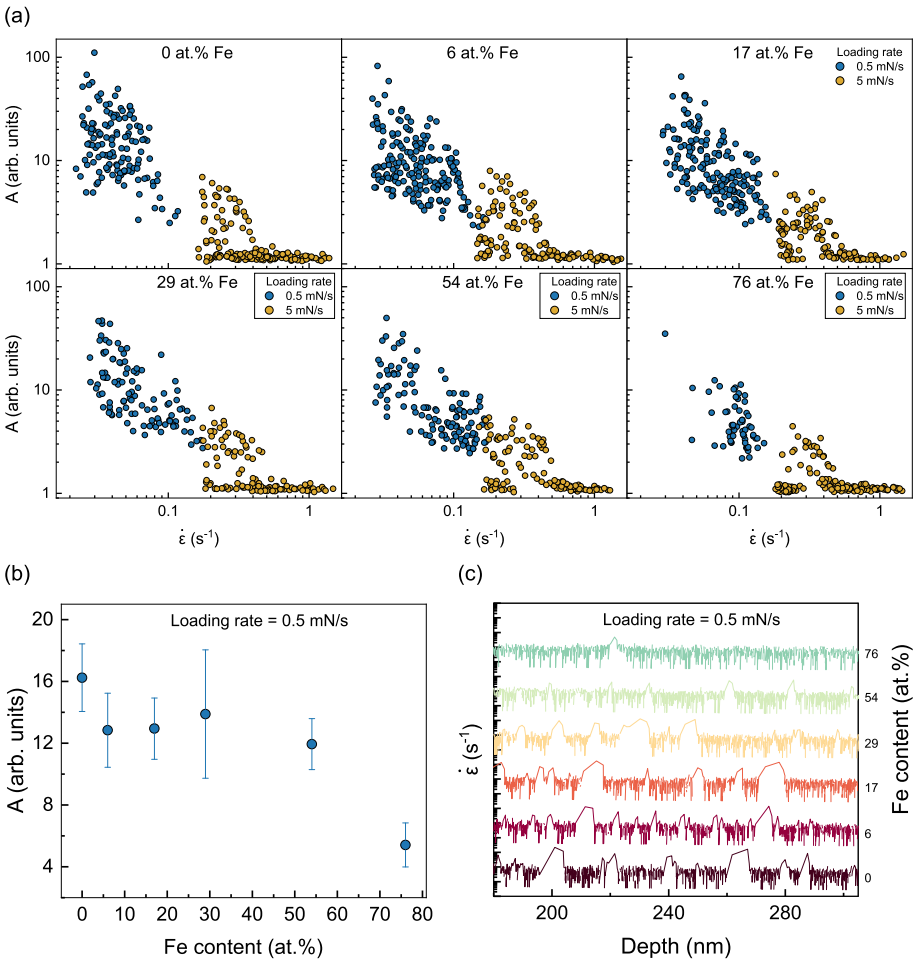

Fig. 8. Characterization of strain-rate dependent deformation. (a) The height (A) of strain rate peaks during pop-in events as a function of $\dot{\varepsilon}_i$, indentation strain rate. (b) Compositional dependence of A at a loading rate of 0.5 mN/s (c) $\dot{\varepsilon}_i$ as a function of indentation depth for $(Zr_{34}Cu_{66})_{100-x}Fe_x$ TFMGs with various Fe content at a loading rate of 0.5 mN/s.

10,2>, whose fraction surpasses that of ideal icosahedra. At high Fe content, chemical and size mismatches may hinder ideal 12-fold packing, forcing the structure to adopt a broader range of polyhedra to pack efficiently, aligning with observations for Fe-based MGs, in which Fe-rich compositions are dominated by distorted rather than perfect icosahedra. For instance, in FeSiBP BMGs, <0,1,10,2> clusters prevail, while the fraction of <0,0,12,0> motifs is low [87], while increasing Fe, the motif distribution broadens, the fraction of dominant polyhedra decreases, and the fraction of less favored types increases, indicating enhanced structural heterogeneity and packing hindrance [68]. The initial increase and subsequent decrease of icosahedral order suggest that additions of Fe below 29 at.% may enhance topological ordering and glass stability of the Zr-Cu system in agreement with Ref. [44], whereas higher Fe contents reduce icosahedral order and indicate the onset of structural instability.

Finally, APT reveals nanoscale segregation at 76 at.% Fe: Cu-rich clusters with a diameter up to several nanometers form within the Fe-rich matrix, unlike the homogenous elemental distribution in $Zr_{34}Cu_{66}$. The formation of nanoclusters reflects the increased instability of the amorphous structure at high Fe content, where the driving force for structural rearrangement becomes significant. At 76 at.% Fe, the Zr-Cu-Fe system approaches the predicted limit of glass formation (Fig. 1b), and nanoscale heterogeneity represents an early stage of destabilization.

These observations are consistent with the behavior of some TFMGs alloyed with immiscible elements, where amorphous structure confirmed by XRD does not necessarily imply chemical homogeneity. For Cu-Nb [34] and Ag-Ni [35], XRD and TEM suggested amorphous structures, whereas APT or atomic-level structural analysis based on extended x-ray absorption fine structures revealed nanoscale phase separation or spinodal-like chemical heterogeneity on an extremely fine scale, respectively. Annealed Cu-Ta TFMGs similarly show spinodal decomposition into Cu-rich and Ta-rich regions [36]. In contrast, ZrCuTi-Ta TFMGs can retain a supersaturated amorphous structure up to ~75 at.% Ta. Thus, alloying with immiscible element can produce in TFMGs may result in different metastable states, ranging from supersaturated amorphous solid solutions to structures with nanoscale chemical separation. In the present Zr-Cu-Fe TFMGs, formation of Cu-rich clusters corresponds to the latter case and indicate chemical destabilization of the amorphous phase rather than crystallization.

Despite the immiscibility between Cu and Fe [88], the $(Zr_{34}Cu_{66})_{100-x}Fe_x$ TFMGs remain amorphous across a broad compositional window, extending up to 76 at.% Fe. This behavior is unexpected compared to melt-spun ribbons, showing a much narrower glass-forming range [40]. Such improved glass-forming ability of TFMGs can be explained by extremely high cooling rates up to 10^{12} K/s during magnetron sputtering [14], significantly exceeding those reported for melt spinning, where typical rates are ~10^5 - 10^6 K/s [89]. Under such conditions, elemental redistribution and nucleation of crystalline phases become suppressed. In addition, the presence of Zr likely favors homogeneity when present in sufficient amounts, due to its negative ΔH_{mix} with Cu and Fe [71]. However, at 76 at.% Fe, Zr concentration seems to be insufficient to suppress Cu-Fe repulsion, and thermodynamic calculations show a minimal free-energy difference between the glassy and crystalline states (Fig. 1b). At this concentration of Fe, instability does

not occur via crystallization but instead through nanoscale phase separation and formation of Cu-rich clusters. This pathway is consistent with decomposition and segregation reported for rapidly quenched Zr-Cu-Fe ribbons [39].

4.2. Mechanical behavior and deformation mechanisms

The above-mentioned structural features determine the macroscopic mechanical behavior of $(Zr_{34}Cu_{66})_{100-x}Fe_x$ TFMGs. The E of TFMGs increases with the Fe content. PDF and XRD analyses indicate that Fe addition, via substitution of larger Zr and Cu by smaller Fe atoms, leads to a denser atomic packing (Figs. 2a and 4a), while partial PDF analysis shows that the Zr-Zr and Cu-Cu bond lengths remain essentially unchanged upon Fe addition (Table S2), indicating that the stiffness of these bonds is retained. Therefore, the increase of E with Fe content primarily originates from the growing fraction of Fe-Fe bonds, whose stiffness is significantly higher [90] than that of Zr-Zr and Cu-Cu bonds [80,91].

This behavior differs from that sputtered ZrCuTi-Ta TFMGs, where immiscible Ta was incorporated into the amorphous matrix up to ~75 at.% without detectable crystalline precipitation. In that system, E remained nearly unchanged up to ~50 at.% Ta and increased only at higher Ta contents, which was attributed to the growing contribution of strong Ta-Ta bonds rather than to pronounced topological changes [37]. This indicates that the elastic response of TFMGs alloyed with immiscible element is governed by local bonding, but the composition range over which this effect emerges is system-dependent.

In contrast to the evolution of E, the H shows a non-monotonic dependence on Fe content, increasing from ~7.9 GPa for $Zr_{34}Cu_{66}$ TFMG to a maximum of ~8.5 GPa at ~29 at.% Fe, followed by a decrease down to ~7.7 GPa at 76 at.% Fe (Fig. 7d). The H peak value correlates with the maximum fraction of shear-resistant icosahedral <0,0,12,0> motifs (Fig. 2c and d), which strengthen the glass atomic structure [68]. Beyond 29 at.% Fe, the fraction of such icosahedra decreases, accompanied by nanoscale chemical segregation and formation of Cu-rich clusters (Fig. 6b), leading to a decrease of H and facilitating plastic flow.

On the other hand, the reduction in H observed at 76 at.%, can be attributed to the formation of chemical heterogeneities in the form of Cu-rich clusters. Stress concentrations arising at the matrix/cluster interfaces are expected to promote the activation of a critical number of STZs at lower applied stresses, thereby causing an earlier onset of plastic flow. Thus, in contrast to the ZrCuTi-Ta system, where no direct evidence of phase separation was observed [37], Cu-Zr-Fe system show that alloying with immiscible element can either stiffen the amorphous matrix through strong solute-solute bonding or reduce hardness once nanoscale chemical segregation becomes sufficiently developed.

The reduction in COS from ~2.2 to ~1.6% with increasing Fe content up to 54 at.% reflects earlier fracture of stronger and more densely packed glasses. AIMD simulations and experimental characterization (Figs. 2, 4, and 7) reveal that compositions contain a higher fraction of icosahedral motifs, exhibit increased strength, and possess denser atomic packing. Similar relationships between composition-dependent local atomic order, dense packing, hardness, and fracture resistance have been reported for ZrCu TFMGs [76]. Such locally ordered configurations can increase the resistance to shear transformations, but at the same time suppress local atomic rearrangements required for distributed plastic flow. As a result, deformation becomes more prone to localization, leading to earlier crack formation and a lower COS. This is consistent with the macroscopic response of MGs, in which mechanical instability is governed by the activation and interaction of STZs with different local shear moduli and threshold stresses, as well as by synthesis-related defects [92]. Thus, the decrease in COS up to 54 at.% Fe can be attributed to the increasing brittleness of a stronger and more structurally ordered glass [58].

In contrast, the partial recovery of COS to ~2.0% at 76 at.% Fe suggests a change in the balance between atomic-scale ordering and nanoscale chemical heterogeneity. At this composition, the reduced fraction of icosahedral motifs may facilitate local atomic rearrangements and promote STZ activation. Meanwhile Cu-rich nanoclusters introduce nanoscale chemical heterogeneity into the amorphous matrix. Such heterogeneities can redistribute local stresses, promote more spatially distributed shear activity, and hinder rapid crack coalescence [7,93]. This interpretation is supported by the lower final crack density observed for the 76 at.% Fe film (Fig. 7), indicating a transition from highly localized fracture toward a more distributed accumulation of deformation.

Nanoindentation revealed a clear transition in SBs dynamics with Fe content increasing. Serration amplitude gradually decreases from ~16 down to ~12 in the Fe concentration range 0-52 at.% and then drops to ~5 in TFMG with 76 at.% Fe (Fig. 8a). Indentation curves appear smoother in the latter sample, indicating more homogeneous flow. Increasing the Fe content leads to reduced average interatomic spacing, suggesting lower free volume in $(Zr_{34}Cu_{66})_{100-x}Fe_x$ TFMGs. Nevertheless, the variation in the magnitude of serrations observed within the compositional range of 0 to 54 at.% Fe is minimal (Fig. 8b), indicating that changes in chemical composition or free volume cannot explain the trend to more uniform deformation at high Fe concentration. Instead, the activation volume V reaches a minimum (~47 Å^3) at 29 at.% Fe, implying that plastic deformation is governed by relatively small flow units. For Fe concentrations exceeding ~29 at.%, an increase in the activation volume is observed, indicating bigger shear events. This behavior reflects a transition from localized shear transformations toward more collective and spatially extended rearrangements, consistent with a more distributed deformation mode resulting in smoother deformation curves (Fig. 8).

Based on the presented results, the deformation behavior of $(Zr_{34}Cu_{66})_{100-x}Fe_x$ TFMGs can be described in terms of nanoscale structural and chemical heterogeneities. Compositional tuning driven by the immiscibility between Cu and Fe enables control over the local heterogeneity, ranging from enhanced SRO at intermediate Fe concentration to nanoscale phase separation in the form of Cu-rich clusters at high Fe content. By locally modifying stiffness, packing efficiency, and distribution of elements, these heterogeneities define the observed transition in deformation behavior, from localized shear-band activity to more spatially distributed plastic flow [7]. Accordingly, Fig. 9 schematically illustrates possible deformation scenarios by analogy with MGs containing nano-precipitates of crystalline phase [94]. SBs may pass through a cluster if its stiffness is similar to the matrix, wrap around or bypass stiffer ones, or be arrested by sufficiently large or rigid clusters, with potential to initiate new SBs nearby. For the state containing 76 at.% Fe, the Cu-rich clusters may therefore act as local obstacles or

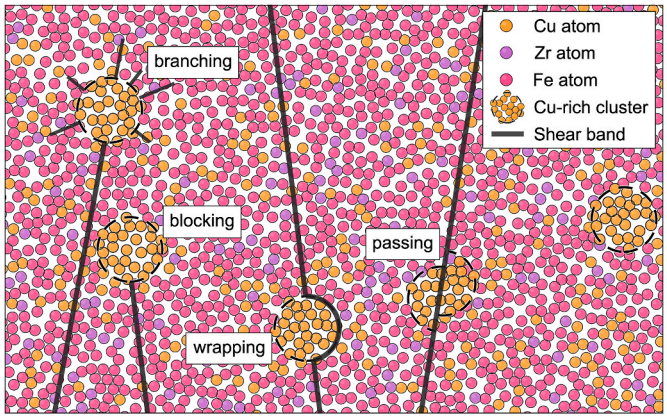

Fig. 9. Schematic of possible SB interactions with local heterogeneities. In $(Zr_{34}Cu_{66})_{24}Fe_{76}$ TFMG, Cu-rich clusters induce various SB interaction scenarios: branching, blocking, wrapping around, and passing.

deflection sites that disrupt uninterrupted SBs propagation and promote SBs branching or multiplication. Together with the reduced fraction of icosahedral motifs, which may facilitate local atomic rearrangements, this cluster-induced heterogeneity can redistribute deformation over a larger volume and delay rapid crack coalescence. Although such interactions cannot be directly resolved in the present experiments, this interpretation is consistent with the lower final crack density and the recovery of COS to ~2.0% observed for the state containing 76 at.% Fe. These results indicate that the presence and characteristics of nanoscale heterogeneities provides a parameter for tailoring the mechanical behavior, making controlled alloying with immiscible elements a promising nanoengineering pathway for TFMGs.

5. Conclusions

Our work demonstrates that alloying $Zr_{34}Cu_{66}$ TFMG with Fe over a compositional range of 0-76 at.% induces significant modifications in both atomic structure and mechanical behavior. Specifically, we show:

- $(Zr_{34}Cu_{66})_{100-x}Fe_x$ retains amorphous structures across the wide compositional range investigated, extending up to 76 at.% Fe in agreement with thermodynamic modeling.
- Increasing Fe content results in a densification of the local atomic structure, demonstrated by a reduction in interatomic distances, and drives a transformation from predominantly 12-fold coordinated Cu-centered and 16-fold coordinated Zr-centered environments toward a more complex and statistically uniform coordination distribution. Moreover, *ab initio* simulations combined with Voronoi analysis reveal a non-monotonic evolution of topological motifs: at intermediate Fe concentrations, there is a pronounced increase in densely packed icosahedral configurations, whereas at Fe contents above 54 at.%, the structure becomes increasingly disordered, with the emergence of low-population polyhedra. We demonstrate the formation of nanoscale Cu-rich clusters in the 76 at.% Fe composition, embedded within a chemically homogeneous amorphous matrix.
- With increasing Fe content, the deformation behavior of $(Zr_{34}Cu_{66})_{100-x}Fe_x$ TFMGs evolves from localized deformation toward a more spatially distributed flow. At low to intermediate Fe concentrations, the increasing fraction of shear-resistant favorable motifs enhances stiffness and hardness but promotes shear localization, as reflected by pronounced serrations, reduced COS, and small activation volumes. In contrast, at high Fe content, the fraction of dominant polyhedra decreases and the emergence of nanoscale chemical heterogeneities in the form of Cu-rich clusters are accompanied by reduced hardness, increased COS, suppressed serration amplitude, and enlarged activation volumes, indicating a transition toward more uniform deformation mode.

Overall, our study shows that nanoscale structural heterogeneities represent an effective design parameter for tailoring local atomic environments and thereby tuning the mechanical properties of TFMGs. Through controlled alloying with an immiscible element, one can promote more uniform deformation behavior, providing a general basis for designing TFMGs with improved mechanical properties.

CRediT authorship contribution statement

Evgeniy Boltynjuk: Data curation, Formal analysis, Investigation, Methodology, Software, Validation, Visualization, Writing – original draft, Writing – review & editing. **Marco Ezequiel:** Data curation, Formal analysis, Investigation, Methodology, Validation, Writing – review & editing. **Francesco Bignoli:** Investigation, Writing – review & editing. **Vahid Tavakkoli:** Investigation, Writing – review & editing. **Ali Ahmadian:** Investigation, Writing – review & editing. **Delphine Chassaing:** Investigation, Writing – review & editing. **Michael Eusterholz:** Investigation, Validation, Writing – review & editing. **Fatih Zighem:** Investigation, Writing – review & editing. **Damien Faurie:** Investigation, Writing – review & editing. **Philippe Djemia:** Data curation, Formal analysis, Funding acquisition, Investigation, Methodology, Project administration, Software, Supervision, Validation, Writing – review & editing. **Horst Hahn:** Conceptualization, Funding acquisition, Methodology, Project administration, Resources, Supervision, Writing – review & editing. **Yulia Ivanisenko:** Conceptualization, Funding acquisition, Methodology, Project administration, Supervision, Writing – review & editing. **Matteo Ghidelli:** Conceptualization, Funding acquisition, Methodology, Project administration, Resources, Supervision, Writing – review & editing.

Declaration of competing interest

The authors declare the following financial interests/personal relationships which may be considered as potential competing interests: Given their role as Editor-in-Chief, H. W. Hahn had no involvement in the peer-review of this article and has no access to information regarding its peer-review. Full responsibility for the editorial process for this article was delegated to another journal editor. If there are other authors, they declare that they have no known competing financial interests or personal relationships that could have appeared to influence the work reported in this paper.

Acknowledgements

E. Boltynjuk, Yu. Ivanisenko, H. Hahn, M. Ghidelli, and P. Djemia acknowledge financial support from the joint Deutsche Forschungsgemeinschaft - Agence Nationale de la Recherche project “EGLASS” (DFG grant number 505805355, ANR grant agreement no. ANR-22-CE92-0026-01). M. Ghidelli acknowledges the financial support of the Agence Nationale de la Recherche under the project “MICRO-HEAs” (grant agreement no ANR-21-CE08–0003–01) as well as of the project Super-Glasses (grant agreement no ANR-24-CE91-0002-02). The authors thank Moritz Ludwig for fruitful discussions. The authors would like to thank the Karlsruhe Nano Micro Facility (KNMFi) at Karlsruhe Institute of Technology (KIT) for the use of facilities.

Appendix A. Supplementary data

Supplementary data to this article can be found online at https://doi.org/10.1016/j.msea.2026.150841.

Supplementary materials

Supplementary material associated with this article is available in the online version.

Data availability

Data will be made available on request.

References

[1] C. Schuh, T. Hufnagel, U. Ramamurty, Mechanical behavior of amorphous alloys, Acta Mater. 55 (2007) 4067–4109, https://doi.org/10.1016/j.actamat.2007.01.052.
[2] M.M. Trexler, N.N. Thadhani, Mechanical properties of bulk metallic glasses, Prog. Mater. Sci. 55 (2010) 759–839, https://doi.org/10.1016/j.pmatsci.2010.04.002.
[3] A.L. Greer, Y.Q. Cheng, E. Ma, Shear bands in metallic glasses, Mater. Sci. Eng. R Rep. 74 (2013) 71–132, https://doi.org/10.1016/j.mser.2013.04.001.
[4] T.C. Hufnagel, C.A. Schuh, M.L. Falk, Deformation of metallic glasses: recent developments in theory, simulations, and experiments, Acta Mater. 109 (2016) 375–393, https://doi.org/10.1016/j.actamat.2016.01.049.
[5] E.S. Park, J.S. Kyeong, D.H. Kim, Phase separation and improved plasticity by modulated heterogeneity in Cu–(Zr,Hf)–(Gd,Y)–Al metallic glasses, Scr. Mater. 57 (2007) 49–52, https://doi.org/10.1016/j.scriptamat.2007.03.008.
[6] J.C. Qiao, Q. Wang, J.M. Pelletier, H. Kato, R. Casalini, D. Crespo, E. Pineda, Y. Yao, Y. Yang, Structural heterogeneities and mechanical behavior of amorphous

alloys, Prog. Mater. Sci. 104 (2019) 250–329, https://doi.org/10.1016/j.pmatsci.2019.04.005.
[7] J. Kim, H.S. Oh, W. Kim, P.-P. Choi, D. Raabe, E.S. Park, Modulation of plastic flow in metallic glasses via nanoscale networks of chemical heterogeneities, Acta Mater. 140 (2017) 116–129, https://doi.org/10.1016/j.actamat.2017.08.002.
[8] B. Sarac, Y.P. Ivanov, A. Chuvilin, T. Schöberl, M. Stoica, Z. Zhang, J. Eckert, Origin of large plasticity and multiscale effects in iron-based metallic glasses, Nat. Commun. 9 (2018), https://doi.org/10.1038/s41467-018-03744-5.
[9] Y. Tang, H. Zhou, H. Lu, X. Wang, Q. Cao, D. Zhang, W. Yang, J.-Z. Jiang, Extra plasticity governed by shear band deflection in gradient metallic glasses, Nat. Commun. 13 (2022) 2120, https://doi.org/10.1038/s41467-022-29821-4.
[10] X.L. Bian, D. Zhao, J.T. Kim, D. Şopu, G. Wang, R. Pippan, J. Eckert, Controlling the distribution of structural heterogeneities in severely deformed metallic glass, Mater. Sci. Eng. A 752 (2019) 36–42, https://doi.org/10.1016/j.msea.2019.02.092.
[11] X. Bian, D. Şopu, G. Wang, B. Sun, J. Bednarčik, C. Gammer, Q. Zhai, J. Eckert, Signature of local stress states in the deformation behavior of metallic glasses, NPG Asia Mater. 12 (2020) 59, https://doi.org/10.1038/s41427-020-00241-4.
[12] J.P. Chu, J.S.C. Jang, J.C. Huang, H.S. Chou, Y. Yang, J.C. Ye, Y.C. Wang, J.W. Lee, F.X. Liu, P.K. Liaw, Y.C. Chen, C.M. Lee, C.L. Li, C. Rullyani, Thin film metallic glasses: unique properties and potential applications, Thin Solid Films 520 (2012) 5097–5122, https://doi.org/10.1016/j.tsf.2012.03.092.
[13] P. Yiu, W. Diyatmika, N. Bönninghoff, Y.-C. Lu, B.-Z. Lai, J.P. Chu, Thin film metallic glasses: properties, applications and future, J. Appl. Phys. 127 (2020) 030901, https://doi.org/10.1063/1.5122884.
[14] D. Turnbull, Metastable structures in metallurgy, Metall. Trans. A 12 (1981) 695–708, https://doi.org/10.1007/BF02648333.
[15] M.-X. Li, S.-F. Zhao, Z. Lu, A. Hirata, P. Wen, H.-Y. Bai, M. Chen, J. Schroers, Y. Liu, W.-H. Wang, High-temperature bulk metallic glasses developed by combinatorial methods, Nature 569 (2019) 99–103, https://doi.org/10.1038/s41586-019-1145-z.
[16] M.-X. Li, Y.-T. Sun, C. Wang, L.-W. Hu, S. Sohn, J. Schroers, W.-H. Wang, Y.-H. Liu, Data-driven discovery of a universal indicator for metallic glass forming ability, Nat. Mater. 21 (2022) 165–172, https://doi.org/10.1038/s41563-021-01129-6.
[17] S.V. Ketov, Y.H. Sun, S. Nachum, Z. Lu, A. Checchi, A.R. Beraldin, H.Y. Bai, W. H. Wang, D.V. Louzguine-Luzgin, M.A. Carpenter, A.L. Greer, Rejuvenation of metallic glasses by non-affine thermal strain, Nature 524 (2015) 200–203, https://doi.org/10.1038/nature14674.
[18] A.H. Balal, X.L. Bian, D.X. Han, B. Huang, S.S. Liao, N. Li, S. Ali, Y.D. Jia, J.C. Qiao, G. Wang, The role of cryogenic treatment in the relaxation behavior of the elastically rejuvenated metallic glasses, Int. J. Plast. 189 (2025) 104356, https://doi.org/10.1016/j.ijplas.2025.104356.
[19] Q. Wang, Y. Yang, H. Jiang, C.T. Liu, H.H. Ruan, J. Lu, Superior tensile ductility in bulk metallic glass with gradient amorphous structure, Sci. Rep. 4 (2014) 4757, https://doi.org/10.1038/srep04757.
[20] D.V. Gunderov, E.V. Boltynjuk, E.V. Ubyivovk, A.V. Lukyanov, A.A. Churakova, A. R. Kilmametov, YuS. Zamula, R.Z. Valiev, Cluster structure in amorphous Ti-Ni-Cu alloys subjected to high-pressure torsion deformation, J. Alloys Compd. 749 (2018) 612–619, https://doi.org/10.1016/j.jallcom.2018.03.357.
[21] X.L. Bian, G. Wang, H.C. Chen, L. Yan, J.G. Wang, Q. Wang, P.F. Hu, J.L. Ren, K. C. Chan, N. Zheng, A. Teresiak, Y.L. Gao, Q.J. Zhai, J. Eckert, J. Beadsworth, K. A. Dahmen, P.K. Liaw, Manipulation of free volumes in a metallic glass through Xe-ion irradiation, Acta Mater. 106 (2016) 66–77, https://doi.org/10.1016/j.actamat.2016.01.002.
[22] M. Ghidelli, A. Orekhov, A.L. Bassi, G. Terraneo, P. Djemia, G. Abadias, M. Nord, A. Béché, N. Gauquelin, J. Verbeeck, J.-P. Raskin, D. Schryvers, T. Pardoen, H. Idrissi, Novel class of nanostructured metallic glass films with superior and tunable mechanical properties, Acta Mater. 213 (2021) 116955, https://doi.org/10.1016/j.actamat.2021.116955.
[23] H. Voigt, A. Rigoni, E. Boltynjuk, M.R. Chellali, B. Tyler, H. Rösner, S. Divinski, H. Hahn, G. Wilde, Evidence for glass–glass interfaces in a columnar Cu–Zr nanoglass, Adv. Funct. Mater. 33 (2023) 2302386, https://doi.org/10.1002/adfm.202302386.
[24] A. Takeuchi, A. Inoue, Classification of bulk metallic glasses by atomic size difference, heat of mixing and period of constituent elements and its application to characterization of the main alloying element, Mater. Trans. 46 (2005) 2817–2829, https://doi.org/10.2320/matertrans.46.2817.
[25] D.H. Kim, W.T. Kim, E.S. Park, N. Mattern, J. Eckert, Phase separation in metallic glasses, Prog. Mater. Sci. 58 (2013) 1103–1172, https://doi.org/10.1016/j.pmatsci.2013.04.002.
[26] Y.-H. Kim, A. Inoue, T. Masumoto, Increase in mechanical strength of al–y–ni amorphous alloys by dispersion of nanoscale fcc-Al particles, Mater. Trans. JIM 32 (1991) 331–338, https://doi.org/10.2320/matertrans1989.32.331.
[27] H.S. Chen, D. Turnbull, Formation, stability and structure of palladium-silicon based alloy glasses, Acta Metall. 17 (1969) 1021–1031, https://doi.org/10.1016/0001-6160(69)90048-0.
[28] C.-P. Peter Chou, D. Turnbull, Transformation behavior of Pd Au Si metallic glasses, J. Non-Cryst. Solids 17 (1975) 169–188, https://doi.org/10.1016/0022-3093(75)90049-6.
[29] K. Osamura, K. Shibue, R. Suzuki, Y. Murakami, S. Takayama, Study of the structure and crystallization of an Fe-17 at % B amorphous alloy, J. Mater. Sci. 16 (1981) 957–967, https://doi.org/10.1007/BF00542740.
[30] Z.G. Liu, X.J. Wu, Y. Chen, X. Wu, X.Y. Qin, Heterogeneity in Fe82.3Ni1.7B16 glass, J. Non-Cryst. Solids 109 (1989) 262–266, https://doi.org/10.1016/0022-3093(89)90038-0.
[31] C. Antonione, S. Spriano, P. Rizzi, M. Baricco, L. Battezzati, Phase separation in multicomponent amorphous alloys, J. Non-Cryst. Solids 232–234 (1998) 127–132, https://doi.org/10.1016/S0022-3093(98)00486-4.
[32] K.F. Yao, F. Ruan, Y.Q. Yang, N. Chen, Superductile bulk metallic glass, Appl. Phys. Lett. 88 (2006) 122106, https://doi.org/10.1063/1.2187516.
[33] C. Michaelsen, C. Gente, R. Bormann, The thermodynamics of amorphous phases in immiscible systems: the example of sputter-deposited Nb–Cu alloys, J. Appl. Phys. 81 (1997) 6024–6030, https://doi.org/10.1063/1.364451.
[34] R. Banerjee, A. Puthucode, S. Bose, P. Ayyub, Nanoscale phase separation in amorphous immiscible copper-niobium alloy thin films, Appl. Phys. Lett. 90 (2007), https://doi.org/10.1063/1.2429017.
[35] J.H. He, H.W. Sheng, P.J. Schilling, C.-L. Chien, E. Ma, Amorphous structures in the immiscible Ag-Ni system, Phys. Rev. Lett. 86 (2001) 2826–2829, https://doi.org/10.1103/PhysRevLett.86.2826.
[36] C.M. Müller, A.S. Sologubenko, S.S.A. Gerstl, R. Spolenak, On spinodal decomposition in Cu–34 at.% Ta thin films – an atom probe tomography and transmission electron microscopy study, Acta Mater. 89 (2015) 181–192, https://doi.org/10.1016/j.actamat.2015.01.073.
[37] H.S. Chou, J.C. Huang, L.W. Chang, Mechanical properties of ZrCuTi thin film metallic glass with high content of immiscible tantalum, Surf. Coat. Technol. 205 (2010) 587–590, https://doi.org/10.1016/j.surfcoat.2010.07.042.
[38] I. Kaban, P. Jóvári, M. Stoica, N. Mattern, J. Eckert, W. Hoyer, B. Beuneu, On the atomic structure of Zr_{60} Cu_{20} Fe_{20} metallic glass, J. Phys. Condens. Matter 22 (2010) 404208, https://doi.org/10.1088/0953-8984/22/40/404208.
[39] X. Sun, J. He, B. Chen, L. Zhang, H. Jiang, J. Zhao, H. Hao, Microstructure formation and electrical resistivity behavior of rapidly solidified cu-fe-zr immiscible alloys, J. Mater. Sci. Technol. 44 (2020) 201–208, https://doi.org/10.1016/j.jmst.2019.10.038.
[40] T.L. Wang, B.X. Liu, Glass forming ability of the fe–zr–cu system studied by thermodynamic calculation and ion beam mixing, J. Alloys Compd. 481 (2009) 156–160, https://doi.org/10.1016/j.jallcom.2009.02.138.
[41] S. Sengul, M. Celtek, U. Domekeli, Molecular dynamics simulations of glass formation and atomic structures in Zr60Cu20Fe20 ternary bulk metallic alloy, Vacuum 136 (2017) 20–27, https://doi.org/10.1016/j.vacuum.2016.11.018.
[42] N. Zou, H.-J. Lu, P.-W. Gu, J.-Y. Wang, X.-K. Feng, J.-Y. Shen, Y.-L. He, L. Li, X.-G. Lu, Thermodynamic assessment and glass forming ability prediction of the Zr-Fe-Cu system, Calphad 64 (2019) 175–184, https://doi.org/10.1016/j.calphad.2018.12.007.
[43] S. Michalik, K. Saksl, P. Sovák, K. Csach, J.Z. Jiang, Crystallization of Zr60Fe20Cu20 amorphous alloy, J. Alloys Compd. 478 (2009) 441–446, https://doi.org/10.1016/j.jallcom.2008.11.083.
[44] Z. Hao, K. Qin, K. Song, C. Cao, Effect of Fe addition on glass-forming ability, thermal stability of B2 CuZr phase and crystallization kinetics for CuZr-based amorphous alloys, J. Mater. Res. Technol. 15 (2021) 6464–6475, https://doi.org/10.1016/j.jmrt.2021.11.093.
[45] J.M. López, J.A. Alonso, L.J. Gallego, Determination of the glass-forming concentration range in binary alloys from a semiempirical theory: application to Zr-based alloys, Phys. Rev. B 36 (1987) 3716–3722, https://doi.org/10.1103/physrevb.36.3716.
[46] G.J. Van Der Kolk, A.R. Miedema, A.K. Niessen, On the composition range of amorphous binary transition metal alloys, J. Common Met. 145 (1988) 1–17, https://doi.org/10.1016/0022-5088(88)90257-3.
[47] C.H. Li, C. Poltronieri, G. Abadias, P. Djemia, Computational approach to identify structural and elastic relationship in metastable crystalline and amorphous alloy thin films: Mo1-xNix and Mo1-xSix case studies, Surf. Coat. Technol. 475 (2023) 130168, https://doi.org/10.1016/j.surfcoat.2023.130168.
[48] G. Kresse, J. Furthmüller, Efficient iterative schemes for*ab initio*total-energy calculations using a plane-wave basis set, Phys. Rev. B 54 (1996) 11169–11186, https://doi.org/10.1103/physrevb.54.11169.
[49] A. Stukowski, Visualization and analysis of atomistic simulation data with OVITO–the open visualization tool, Model. Simulat. Mater. Sci. Eng. 18 (2010) 015012, https://doi.org/10.1088/0965-0393/18/1/015012.
[50] X. Mu, M.R. Chellali, E. Boltynjuk, D. Gunderov, R.Z. Valiev, H. Hahn, C. Kübel, Y. Ivanisenko, L. Velasco, Unveiling the local atomic arrangements in the shear band regions of metallic glass, Adv. Mater. 33 (2021) 2007267, https://doi.org/10.1002/adma.202007267.
[51] T. Philippe, F. De Geuser, S. Duguay, W. Lefebvre, O. Cojocaru-Mirédin, G. Da Costa, D. Blavette, Clustering and nearest neighbour distances in atom-probe tomography, Ultramicroscopy 109 (2009) 1304–1309, https://doi.org/10.1016/j.ultramic.2009.06.007.
[52] L.T. Stephenson, M.P. Moody, P.V. Liddicoat, S.P. Ringer, New techniques for the analysis of fine-scaled clustering phenomena within Atom Probe Tomography (APT) data, Microsc. Microanal. 13 (2007) 448–463, https://doi.org/10.1017/s1431927607070900.
[53] E. Boltynjuk, F. Bignoli, S.H. Nandam, D. Faurie, A. Welle, R. Kruk, P. Djemia, H. Hahn, Y. Ivanisenko, M. Ghidelli, Nanocolumnar ZrCu thin film metallic glass with tailored mechanical and electrical properties, Thin Solid Films 825 (2025) 140748, https://doi.org/10.1016/j.tsf.2025.140748.
[54] N. Lu, X. Wang, Z. Suo, J. Vlassak, Metal films on polymer substrates stretched beyond 50%, Appl. Phys. Lett. 91 (2007) 221909 https://doi.org/10.1063/1.2817234.
[55] P. Kreiml, M. Rausch, V.L. Terziyska, H. Köstenbauer, J. Winkler, C. Mitterer, M. J. Cordill, Electro-mechanical behavior of Al/Mo bilayers studied with in situ straining methods, Thin Solid Films 665 (2018) 131–136, https://doi.org/10.1016/j.tsf.2018.07.054.

[56] D. Faurie, N. Girodon-Boulandet, A. Kaladjian, F. Challali, G. Abadias, P. Djemia, Setup for high-temperature surface Brillouin light scattering: application to opaque thin films and coatings, Rev. Sci. Instrum. 88 (2017) 023903, https://doi.org/10.1063/1.4975637.
[57] W.C. Oliver, G.M. Pharr, Measurement of hardness and elastic modulus by instrumented indentation: advances in understanding and refinements to methodology, J. Mater. Res. 19 (2004) 3–20, https://doi.org/10.1557/jmr.2004.19.1.3.
[58] W.L. Johnson, K. Samwer, A universal criterion for plastic yielding of metallic glasses with a (T/T g) 2/3 temperature dependence, Phys. Rev. Lett. 95 (2005) 195501, https://doi.org/10.1103/PhysRevLett.95.195501.
[59] C.A. Schuh, T.G. Nieh, A nanoindentation study of serrated flow in bulk metallic glasses, Acta Mater. 51 (2003) 87–99, https://doi.org/10.1016/S1359-6454(02)00303-8.
[60] N. Mattern, A. Schöps, U. Kühn, J. Acker, O. Khvostikova, J. Eckert, Structural behavior of CuxZr100−x metallic glass (x=35−70), J. Non-Cryst. Solids 354 (2008) 1054–1060, https://doi.org/10.1016/j.jnoncrysol.2007.08.035.
[61] S.Q. Wu, C.Z. Wang, S.G. Hao, Z.Z. Zhu, K.M. Ho, Energetics of local clusters in Cu64.5Zr35.5 metallic liquid and glass, Appl. Phys. Lett. 97 (2010), https://doi.org/10.1063/1.3464164.
[62] F. Li, H. Zhang, X. Liu, C. Yu, Z. Lu, Effects of cooling rate on the atomic structure of Cu64Zr36 binary metallic glass, Comput. Mater. Sci. 141 (2018) 59–67, https://doi.org/10.1016/j.commatsci.2017.09.026.
[63] J. Ding, E. Ma, M. Asta, R.O. Ritchie, Second-nearest-neighbor correlations from connection of atomic packing motifs in metallic glasses and liquids, Sci. Rep. 5 (2015), https://doi.org/10.1038/srep17429.
[64] K.G. Soni, J.P. Anadani, M.B. Vahiya, K.N. Lad, Compositional effects on structure, dynamics, thermodynamic and mechanical properties of Zr-Cu-Al alloys, J. Non-Cryst. Solids 667 (2025) 123749, https://doi.org/10.1016/j.jnoncrysol.2025.123749.
[65] A. Okabe (Ed.), Spatial Tessellations: Concepts and Applications of Voronoi Diagrams, second ed., Wiley, Chichester, 2000.
[66] Y.Q. Cheng, E. Ma, Atomic-level structure and structure–property relationship in metallic glasses, Prog. Mater. Sci. 56 (2011) 379–473, https://doi.org/10.1016/j.pmatsci.2010.12.002.
[67] D. Ma, A.D. Stoica, X.-L. Wang, Z.P. Lu, M. Xu, M. Kramer, Efficient local atomic packing in metallic glasses and its correlation with glass-forming ability, Phys. Rev. B 80 (2009), https://doi.org/10.1103/physrevb.80.014202.
[68] Y.Q. Cheng, A.J. Cao, H.W. Sheng, E. Ma, Local order influences initiation of plastic flow in metallic glass: effects of alloy composition and sample cooling history, Acta Mater. 56 (2008) 5263–5275, https://doi.org/10.1016/j.actamat.2008.07.011.
[69] Y. Zhang, J. Pang, Q. Xiang, D. Yang, Y. Ren, X. Li, K. Qiu, The effect of the volume fraction of nanocrystals on the brittleness of Fe-based amorphous/nanocrystalline alloys simulated by molecular dynamics, J. Non-Cryst. Solids 625 (2024) 122735, https://doi.org/10.1016/j.jnoncrysol.2023.122735.
[70] Y. Wang, A. Takeuchi, A. Makino, Y. Liang, Y. Kawazoe, Atomic packing and diffusion in Fe85Si2B9P4 amorphous alloy analyzed by *ab initio* molecular dynamics simulation, J. Appl. Phys. 117 (2015), https://doi.org/10.1063/1.4907230.
[71] Q. Yu, X.D. Wang, H.B. Lou, Q.P. Cao, J.Z. Jiang, Atomic packing in Fe-based metallic glasses, Acta Mater. 102 (2016) 116–124, https://doi.org/10.1016/j.actamat.2015.09.001.
[72] M. Apreutesei, C. Esnouf, A. Billard, P. Steyer, Impact of local nanocrystallization on mechanical properties in the Zr-59 at.% Cu metallic glass thin film, Mater. Des. 108 (2016) 8–12, https://doi.org/10.1016/j.matdes.2016.06.081.
[73] X-ray Diffraction: in Crystals, Imperfect Crystals, and Amorphous Bodies, n.d.
[74] B. Gault, A. Chiaramonti, O. Cojocaru-Mirédin, P. Stender, R. Dubosq, C. Freysoldt, S.K. Makineni, T. Li, M. Moody, J.M. Cairney, Atom probe tomography, Nat. Rev. Methods Primers 1 (2021), https://doi.org/10.1038/s43586-021-00047-w.
[75] T. Jörg, D. Music, F. Hauser, M.J. Cordill, R. Franz, H. Köstenbauer, J. Winkler, J. M. Schneider, C. Mitterer, Deformation behavior of Re alloyed Mo thin films on flexible substrates: in situ fragmentation analysis supported by first-principles calculations, Sci. Rep. 7 (2017), https://doi.org/10.1038/s41598-017-07825-1.
[76] A. Brognara, J.P. Best, P. Djemia, D. Faurie, G. Dehm, M. Ghidelli, Effect of composition and nanostructure on the mechanical properties and thermal stability of Zr100-xCux thin film metallic glasses, Mater. Des. 219 (2022) 110752, https://doi.org/10.1016/j.matdes.2022.110752.
[77] P. Zeman, M. Zítek, Š. Zuzjaková, R. Čerstvý, Amorphous Zr-Cu thin-film alloys with metallic glass behavior, J. Alloys Compd. 696 (2017) 1298–1306, https://doi.org/10.1016/j.jallcom.2016.12.098.
[78] S. Comby-Dassonneville, T. Venot, A. Borroto, E. Longin, C. Der Loughian, B. Ter Ovanessian, M.-A. Leroy, J.-F. Pierson, P. Steyer, ZrCuAg thin-film metallic glasses: toward biostatic durable advanced surfaces, ACS Appl. Mater. Interfaces 13 (2021) 17062–17074, https://doi.org/10.1021/acsami.1c01127.
[79] M. Apreutesei, P. Steyer, L. Joly-Pottuz, A. Billard, J. Qiao, S. Cardinal, F. Sanchette, J.M. Pelletier, C. Esnouf, Microstructural, thermal and mechanical behavior of co-sputtered binary Zr–Cu thin film metallic glasses, Thin Solid Films 561 (2014) 53–59, https://doi.org/10.1016/j.tsf.2013.05.177.
[80] B.N. Galimzyanov, M.A. Doronina, A.V. Mokshin, Machine learning-based prediction of elastic properties of amorphous metal alloys, Phys. Stat. Mech. Its Appl. 617 (2023) 128678, https://doi.org/10.1016/j.physa.2023.128678.
[81] C. Poltronieri, A. Brognara, F. Bignoli, S. Evertz, P. Djemia, D. Faurie, F. Challali, C. H. Li, L. Belliard, G. Dehm, J.P. Best, M. Ghidelli, Mechanical properties and thermal stability of ZrCuAlx thin film metallic glasses: experiments and first-principle calculations, Acta Mater. 258 (2023) 119226, https://doi.org/10.1016/j.actamat.2023.119226.
[82] Y. Ma, G.J. Peng, W.F. Jiang, H. Chen, T.H. Zhang, Nanoindentation study on shear transformation zone in a CuZrAl metallic glassy film with different thickness, J. Non-Cryst. Solids 442 (2016) 67–72, https://doi.org/10.1016/j.jnoncrysol.2016.03.016.
[83] Y. Wang, J. Zhang, K. Wu, G. Liu, D. Kiener, J. Sun, Nanoindentation creep behavior of Cu–Zr metallic glass films, Mater. Res. Lett. 6 (2018) 22–28, https://doi.org/10.1080/21663831.2017.1383946.
[84] S.Y. Wu, S.H. Wei, G.Q. Guo, J.G. Wang, L. Yang, Structural mechanism of the enhanced glass-forming ability in multicomponent alloys with positive heat of mixing, Sci. Rep. 6 (2016) 38098, https://doi.org/10.1038/srep38098.
[85] M. Celtek, U. Domekeli, S. Sengul, C. Canan, Effects of Ag or Al addition to CuZr-based metallic alloys on glass formation and structural evolution: a molecular dynamics simulation study, Intermetallics 128 (2021) 107023, https://doi.org/10.1016/j.intermet.2020.107023.
[86] Y.Q. Cheng, H.W. Sheng, E. Ma, Relationship between structure, dynamics, and mechanical properties in metallic glass-forming alloys, Phys. Rev. B 78 (2008) 014207, https://doi.org/10.1103/PhysRevB.78.014207.
[87] H. Chen, B. Dong, S. Zhou, X. Li, J. Qin, Structural, magnetic, and electronic properties of Fe82Si4B10P4 metallic glass, Sci. Rep. 8 (2018) 5680, https://doi.org/10.1038/s41598-018-23952-9.
[88] C.-X. Peng, K.-K. Song, L. Wang, D. Şopu, S. Pauly, J. Eckert, Correlation between structural heterogeneity and plastic deformation for phase separating FeCu metallic glasses, Sci. Rep. 6 (2016) 34340, https://doi.org/10.1038/srep34340.
[89] J. Qiao, H. Jia, P.K. Liaw, Metallic glass matrix composites, Mater. Sci. Eng. R Rep. 100 (2016) 1–69, https://doi.org/10.1016/j.mser.2015.12.001.
[90] H.X. Li, Z.C. Lu, S.L. Wang, Y. Wu, Z.P. Lu, Fe-based bulk metallic glasses: glass formation, fabrication, properties and applications, Prog. Mater. Sci. 103 (2019) 235–318, https://doi.org/10.1016/j.pmatsci.2019.01.003.
[91] M. Apreutesei, P. Djemia, L. Belliard, G. Abadias, C. Esnouf, A. Billard, P. Steyer, Structural-elastic relationships of Zr-TL (TL = Cu, Co, Ni) thin films metallic glasses, J. Alloys Compd. 707 (2017) 126–131, https://doi.org/10.1016/j.jallcom.2016.12.208.
[92] D. Pan, A. Inoue, T. Sakurai, M.W. Chen, Experimental characterization of shear transformation zones for plastic flow of bulk metallic glasses, Proc. Natl. Acad. Sci. 105 (2008) 14769–14772, https://doi.org/10.1073/pnas.0806051105.
[93] Y. Gu, X. Han, F. Yan, L. Li, The strain rate sensitivity of heterogeneous thin film metallic glasses: interplay between Nanoscale heterogeneity and dynamic plasticity, Front. Mater. 9 (2022) 925096, https://doi.org/10.3389/fmats.2022.925096.
[94] T. Brink, M. Peterlechner, H. Rösner, K. Albe, G. Wilde, Influence of crystalline nanoprecipitates on shear-band propagation in cu-zr-based metallic glasses, Phys. Rev. Appl. 5 (2016) 054005, https://doi.org/10.1103/PhysRevApplied.5.054005.